

# Two domain decomposition methods, SDIM and CBFM, for scattering from a two-dimensional perfectly conducting rough surface: comparison and parametric study

CHRISTOPHE BOURLIER,<sup>1,\*</sup> Y. ARENCIBIA NOA,<sup>1</sup> GILDAS KUBICKÉ,<sup>2</sup> AND S. BELLEZ<sup>3</sup>

<sup>1</sup>Institut d'Electronique et des Technologies du numéRique, IETR Laboratory, UMR CNRS 6164, University of Nantes, La Chantrerie, Nantes, France

<sup>2</sup>DGA/DT/MI (Direction Générale de l'Armement-Direction Technique-Maîtrise de l'Information), CGN1 division, BP7, 35998 Rennes cedex 09, France

<sup>3</sup>CMN (Constructions Mécaniques de Normandie), 51 Rue de la Bretonnière, 50100 Cherbourg-Octeville, France

\*Corresponding author: christophe.bourlier@univ-nantes.fr

Received 15 May 2020; revised 16 July 2020; accepted 20 July 2020; posted 21 July 2020 (Doc. ID 397764); published 0 MONTH 0000

**This paper focuses on the two domain decomposition methods, the subdomain decomposition iterative method (SDIM) and the characteristics basis function method (CBFM), combined with adaptive cross approximation (ACA) to compute the normalized radar cross section (NRCS) from a perfectly conducting two-dimensional (2D) randomly rough surface. The 3D electromagnetic problem is solved from the electric field integral equation discretized by the Galerkin method of moments with the Rao–Wilton–Glisson basis functions. In addition, a parametric study versus the number of blocks, the number of overlapping edges, the thresholds of recompressed ACA (RACA; ACA combined with two QR decompositions and truncated by a SVD procedure, also named ACA-SVD or ACA-TSVD), and the parameters inherent to the CBFM is investigated. The complexity of the two methods is also addressed.** © 2020 Optical Society of America

<https://doi.org/10.1364/JOSAA.397764>

## 1. INTRODUCTION

The study of wave scattering from randomly rough surfaces is a subject of great interest. The applications of such research concern many areas that include remote sensing, radar surveillance, optics, and ocean acoustics. Classically, two families of approaches have been developed to solve this issue. The first one is based on asymptotic methods [1–4], in which simplifying assumptions are introduced to obtain a closed-form expression of the scattered field. The second family is based on rigorous approaches, such as the method of moments (MoM) [5–8].

In this paper, to calculate the scattered field by a perfectly conducting two-dimensional (2D) rough surface, the electric field integral equation (EFIE) is discretized by the Galerkin method MoM with the Rao–Wilton–Glisson (RWG) basis functions. To solve the resulting linear system, direct solvers like the LU decomposition can be employed, but it is limited by the size of the problem. Then, iterative solvers like the conjugate gradient and their improved versions [8,9] have been developed to solve larger size problems and to decrease the computing time. In addition, to expedite the matrix-vector products, accelerations are hybridized, like the fast multipole method (FMM) [10] and

the far-field approximation [11]. Since the 2000s, the team of Tsang *et al.* [12], has also extended the original version of the sparse matrix canonical-grid method with the pulse basis function and point matching method [13,14] to the RWG MoM [15–17].

Another family [18–21] to rigorously solve problems involving a large number of unknowns can be applied and is based on domain decomposition methods. These methods also provide a fast iterative solution of the problem based on the subdivision of the entire geometry into several subdomains (blocks). In this way, the MoM impedance matrix is partitioned and the solution is then obtained from an iterative scheme involving the local impedance submatrices. The characteristics basis function method (CBFM) [18] and the subdomain decomposition iterative method (SDIM) [20] are two domain decomposition methods that are well adapted to the problem addressed in this paper: rough surface scattering.

In recent years, rank-based methods have attracted considerable attention because they are kernel independent and can be easily integrated into a variety of MoM codes (see [22] for a brief review). The adaptive cross approximation (ACA) algorithm, published by Bebendorf in 2000 [23] and next applied

by Zhao *et al.* [24] for electromagnetic problems, is an efficient technique to generate a compressed approximate representation of the low rank of off-diagonal blocks. They represent interactions between spatially separated groups of basis functions that are usually rank deficient. In [25,26], this compression is generalized to the whole impedance matrix.

This paper focuses on SDIM and CBFM combined with ACA to compute the normalized radar cross section (NRCS) from a perfectly conducting randomly rough 2D surface. For a 1D rough surface, [20,27] showed that SDIM is efficient when the geometry is a rough surface. CBFM, on the other hand, is efficient for scattering and radiation 3D problems, for which few papers have been published [28,29] to date to the best of our knowledge for a rough surface.

Preliminary comparisons between CBFM and SDIM are presented in [30], for which a square rough surface of area  $(10\lambda_0)^2$  is considered. In addition, for the CBFM, the primary and secondary basis functions (PBFs and SBFs, respectively) are computed from a single incident plane wave, which implies that the results do not match with those computed from a direct LU inversion of the impedance matrix. In this paper, the PBFs are computed from a collection of  $N_{\text{IPW}}$  bipolarized plane waves [31], for which the integer  $N_{\text{IPW}}$  is well chosen. In addition, a parametric study versus the number of blocks, the number of overlapping edges, the thresholds of recompressed ACA (RACA) and the parameters inherent to the CBFM ( $N_{\text{IPW}}, \dots$ ) is addressed. RACA combines ACA with two QR decompositions truncated by a SVD procedure, also named ACA-SVD or ACA-TSVD [22,26,32].

The paper has four sections. Section 2 briefly presents the SDIM, the CBFM, and the RACA algorithms. Section 3 compares the NRCS computed from the SDIM-RACA and CBFM-RACA to the parameters of each method and Section 4 gives concluding remarks.

## 2. SDIM, CBFM, AND RACA ALGORITHMS

### A. MoM

In this paper, to compute the field scattered by a perfectly conducting object, the EFIE is solved from the MoM. In addition, the Galerkin method is applied with the RWG basis functions. This approach leads to a solution for the linear system  $\bar{\mathbf{Z}}\mathbf{X} = \mathbf{b}$ , where  $\bar{\mathbf{Z}}$  is the impedance matrix,  $\mathbf{b}$  is a vector related to the incident wave, and  $\mathbf{X}$  is the unknown vector. The time convention  $e^{-j\omega t}$  is used throughout this paper.

The element  $Z_{m,n}$  of the impedance matrix  $\bar{\mathbf{Z}}$ , corresponding to the interaction between two edges  $m$  (observation) and  $n$  (source) of a facet couple  $(p, q)$  is expressed as [8]

$$Z_{m,n} = \frac{c_{m,n}}{A_p A_q} \iint_{T_p} \iint_{T_q} \times \left[ \frac{1}{4} \boldsymbol{\rho}_m^p \cdot \boldsymbol{\rho}_n^q - \frac{1}{k^2} \right] \frac{e^{-jk_0 D_{p,q}}}{D_{p,q}} dR_p dR_q, \quad (1)$$

where  $c_{m,n} = L_m L_n s_{m,n} / (4\pi)$ , in which  $\{L_{m,n}\}$  are the edge lengths and  $s_{m,n} = \pm 1$ ,  $\{A_{p,q}\}$  are the triangle areas;  $\boldsymbol{\rho}_{m,n}^{p,q} = \mathbf{V}_{m,n}^{p,q} - \mathbf{R}_{p,q}$  in which  $\mathbf{V}_{m,n}^{p,q}$  is the position vector of the vertex unshared by the edge  $(m, n)$  and belonging to the

facet  $(p, q)$ . In addition,  $D_{p,q} = \|\mathbf{R}_p - \mathbf{R}_q\|$  and  $k_0$  is the wave number that equals  $2\pi/\lambda_0$ , where  $\lambda_0$  is the wavelength in free space. The two numerical integrations over the triangles  $\{T_{p,q}\}$  are done from the Gauss-Legendre method, in which one or three points are used. The singularity, which occurs for  $D_{p,q} = 0$ , is computed from the work published by [33] by using six points for the Gauss-Legendre integrations.

A component  $b_n$  of the vector  $\mathbf{b}$  associated to the source edge  $n$  and facet  $q$  is defined as [8]

$$b_n = -\frac{j}{\omega\mu_0} \frac{L_n s_n}{2A_q} \iint_{T_q} \boldsymbol{\rho}_n^q \cdot \hat{\mathbf{p}}_{\text{inc}} \psi_{\text{inc}}(\mathbf{R}_q) dR_q, \quad (2)$$

where  $\omega$  is the wave pulsation and  $\mu_0$  the permeability of the surrounding medium assumed to be a vacuum. In addition,  $\psi_{\text{inc}}$  is the incident wave of polarization  $\hat{\mathbf{p}}_{\text{inc}}$  [either vertical,  $\hat{\mathbf{v}}_{\text{inc}}(V)$ , or horizontal,  $\hat{\mathbf{h}}_{\text{inc}}(H)$ ]. Solving the linear system  $\mathbf{X} = \bar{\mathbf{Z}}^{-1} \mathbf{b}$ , the components  $\{a_n\}$  of the vector  $\mathbf{X}$  are found. The far-field scattered field is then expressed as

$$\mathbf{E}_{\text{sca}}^\infty(\mathbf{R}_0) = -\frac{j\omega\mu_0 e^{-jkR_0}}{8\pi R_0} \sum_{p=1}^{P_{\text{Facet}}} \sum_{m=1}^{M_{\text{Edge}}} \times \frac{L_m a_m s_m}{A_p} \iint_{T_p} \boldsymbol{\rho}_m^p e^{jk_{\text{sca}} \cdot \mathbf{R}_p} dR_p, \quad (3)$$

where  $P_{\text{Facet}}$  is the number of facets (or triangles) and  $M_{\text{Edge}}$  the number of edges associated to the facet  $p$ . In addition,  $R_0$  is the distance from the receiver to the phase origin of the object. The normalized scattering cross section (or dimensionless scattering coefficient) is then expressed as

$$\text{NRCS}_{p_{\text{inc}} p_{\text{sca}}} = \lim_{R_0 \rightarrow \infty} \frac{R_0^2 |\mathbf{E}_{\text{sca}}^\infty \cdot \hat{\mathbf{p}}_{\text{sca}}|^2}{2\eta_0 A_0 P_{\text{inc}}}, \quad (4)$$

where  $A_0 = L_x \times L_y$  is the surface area,  $\eta_0 = 120\pi$  is the wave impedance in free space, and  $P_{\text{inc}}$  is the incident power density,  $p_{\text{inc}} = \{V, H\}$  and  $p_{\text{sca}} = \{V, H\}$ . The subscripts "inc" and "sca" stand for incident and scattered (waves), respectively. The receiver polarization basis  $(\hat{\mathbf{k}}_{\text{sca}}, \hat{\mathbf{v}}_{\text{sca}}, \hat{\mathbf{h}}_{\text{sca}})$  can be defined in a similar way as that of the incident field  $(\hat{\mathbf{k}}_{\text{inc}}, \hat{\mathbf{v}}_{\text{inc}}, \hat{\mathbf{h}}_{\text{inc}})$ , in which  $(\theta_{\text{inc}}, \phi_{\text{inc}})$  and  $(\theta_{\text{sca}}, \phi_{\text{sca}})$  are the incidence and receiver (scattering) angles. To strongly attenuate the edge diffraction by the surface, the well-known incident tapered wave published by Braunish *et al.* [34] will be applied (at the order two) with tapering parameter  $g = L_x/4$  (surface of area  $A_0 = L_x^2$ ). The length  $g$  controls the extent of the incident beam that illuminates the surface.

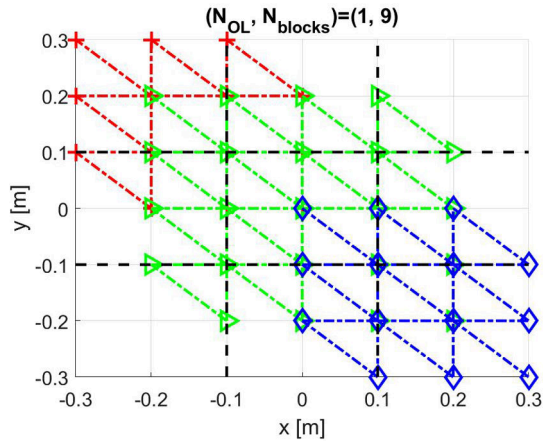
### B. SDIM

Table 1 gives the definition of the notations introduced for the decomposition by blocks, SDIM, CBFM, and ACA, respectively. In addition, Fig. 1 shows an example of decomposition by blocks.

The SDIM begins by dividing the geometry of the object to analyze into  $P$  blocks. The impedance matrix  $\bar{\mathbf{Z}}$  is then

**Table 1. Definition of the Notations Introduced for the Decomposition by Blocks, SDIM, CBFM and ACA, Respectively**

Name	Definition
$N_{\text{Edge}}$	Total number of edges
$N_{\text{Vertex}}$	Total number of vertices
$P = N_{\text{Block}}$	Number of blocks
$N_{\text{Edge,OL}}$	Total number of edges with overlapping
$n_{\text{OL}}$	Exceed edges due to the overlapping
$N_p$	Number of edges of block $p$
$N_{\text{OL},p}$	Number of edges of block $p$ with overlapping
$\bar{N}_{\text{Edge}}$	Mean value of $N_p$ over $p \in [1; P]$
$\bar{N}_{\text{Edge,OL}}$	Mean value of $N_{\text{OL},p}$ over $p \in [1; P]$
$K_{\text{SDIM}}$	SDIM convergence order
$\epsilon_{\text{SDIM}}$	SDIM threshold
$\bar{\tau}_{\text{SDIM}}$	SDIM ACA mean compression rate
$\bar{\tau}_{\text{SDIM,RACA}}$	SDIM RACA mean compression rate
$\bar{N}_{\text{IPW},p}$	CBFM plane wave number of block $p$
$\bar{N}_{\text{IPW}}$	Mean value of $\bar{N}_{\text{IPW},p}$ over $p \in [1; P]$
$\epsilon_{\text{CBFM,SVD}}$	CBFM threshold of the SVD truncation
$\bar{N}_{\text{IPW,SVD},p}$	CBFM plane wave number of block $p$ after SVD truncation
$\bar{N}_{\text{IPW,SVD}}$	Mean value of $\bar{N}_{\text{IPW,SVD},p}$ over $p \in [1; P]$
$n_{\text{IPW}} \geq 1$	Integer defined in Eq. (25)
$\bar{\tau}_{\text{CBFM}}$	CBFM ACA mean compression rate
$\epsilon_{\text{ACA}}$	ACA threshold
$\epsilon_{\text{ACA},1}$	ACA threshold for the adjacent blocks
$\epsilon_{\text{ACA},2}$	ACA threshold for the non-adjacent blocks
$\epsilon_{\text{ACA,SVD}}$	RACA threshold



**Fig. 1.** Edges of the overlapped blocks numbers 1 (red), 4 (green), and 9 (blue).  $N_{\text{Block}} = P = 9$  ( $N_{\text{Block},x} = N_{\text{Block},y} = 3$ ),  $N_{\text{Edge}} = 96$ , number of vertices  $N_{\text{Vertex}} = 49$ , number of triangles (or facets)  $N_{\text{Facet}} = 72$ ,  $A_0 = (0.6\lambda)^2$  ( $L_x = L_y = 0.6\lambda$ ),  $n_{\text{OL}} = 1$  and  $\lambda_0 = 1$  m. The blocks are numbered from top to bottom going from left to right.

$$\begin{bmatrix} \bar{\mathbf{Z}}_{1,1} & \bar{\mathbf{Z}}_{1,2} & \dots & \bar{\mathbf{Z}}_{1,P} \\ \bar{\mathbf{Z}}_{2,1} & \bar{\mathbf{Z}}_{2,2} & \dots & \bar{\mathbf{Z}}_{2,P} \\ \vdots & \vdots & \ddots & \vdots \\ \bar{\mathbf{Z}}_{P,1} & \bar{\mathbf{Z}}_{P,2} & \dots & \bar{\mathbf{Z}}_{P,P} \end{bmatrix} \begin{bmatrix} \mathbf{a}_1 \\ \mathbf{a}_2 \\ \vdots \\ \mathbf{a}_P \end{bmatrix} = \begin{bmatrix} \mathbf{b}_1 \\ \mathbf{b}_2 \\ \vdots \\ \mathbf{b}_P \end{bmatrix}, \quad (5)$$

where  $\bar{\mathbf{Z}}_{p,p}$  are the self-impedance matrix of the block number  $p$  and  $\bar{\mathbf{Z}}_{p_1,p_2}$  are the coupling impedance matrix between the

blocks  $p_1$  and  $p_2$ . In addition, the vectors  $\mathbf{a}_p$  and  $\mathbf{b}_p$  are the vectors  $\mathbf{a}$  and  $\mathbf{b}$  of the block number  $p$ , respectively.

From SDIM [20], the unknown  $\mathbf{a}$  is expressed as

$$\mathbf{a}^{(K_{\text{SDIM}})} \approx \sum_{k=0}^{k=K_{\text{SDIM}}} \mathbf{Y}^{(k)}, \quad (6)$$

where

$$\begin{cases} \mathbf{Y}_{i'}^{(0)} = \bar{\mathbf{Z}}_{i',i'}^{-1} \mathbf{b}_{i'} \\ \mathbf{Y}_{i'}^{(k)} = -\bar{\mathbf{Z}}_{i',i'}^{-1} \sum_{p=1, p \neq i}^P \bar{\mathbf{Z}}_{i',p} \mathbf{Y}_p^{(k-1)} k > 0 \end{cases}, \quad (7)$$

and the vector  $\mathbf{Y}^{(k)} = [\mathbf{Y}_1^{(k)} \mathbf{Y}_2^{(k)} \dots \mathbf{Y}_P^{(k)}]^T$  is built from the characteristic functions associated to the blocks and computed from Eq. (7). The convergence order  $K_{\text{SDIM}}$  is obtained when the relative residual error  $\text{RRE}_{\text{SDIM}}$  satisfies

$$\text{RRE}_{\text{SDIM}} = \frac{\|\mathbf{a}^{(k-1)} - \mathbf{a}^{(k)}\|}{\|\mathbf{a}^{(k)}\|} \leq \epsilon_{\text{SDIM}}, \quad (8)$$

where  $\epsilon_{\text{SDIM}}$  is the SDIM threshold. Typically,  $\epsilon_{\text{SDIM}} = 10^{-2}$ .

It is important to underline that the symbol prime in the subscript of Eq. (7) indicates that the block is enlarged. The vector  $\mathbf{Y}_{i'}^{(k)}$  is obtained from  $\mathbf{Y}_i^{(k)}$  by removing the overlapping edges. The matrix  $\bar{\mathbf{Z}}_{i',j}$  is the coupling matrix between the source block  $j$  and the enlarged block  $i$ . For the vector  $\mathbf{Y}_p^{(k-1)}$ , the overlapped edges are removed to avoid propagation of the non-physical edge currents produced by the finitude of the block.

Unlike a 1D surface [20], for a 2D surface if the blocks are not enlarged, then the SDIM does not converge. The simulations will show that an enlargement of two or three edges (it depends on the size of the block) is enough so that SDIM converges.

From Eq. (7), the complexity of SDIM is

$$\begin{aligned} C_{\text{SDIM}} \approx & P(K_{\text{SDIM}} + 1) \left[ \mathcal{O}(\bar{N}_{\text{Edge,OL}}^3) + \mathcal{O}(\bar{N}_{\text{Edge,OL}}^2) \right] \\ & + K_{\text{SDIM}} P(P-1) \mathcal{O}(\bar{N}_{\text{Edge}} \bar{N}_{\text{Edge,OL}}). \end{aligned} \quad (9)$$

The mean values, indicated by the notation  $\bar{\cdot}$ , are defined as

$$\bar{N}_{\text{Edge,OL}} = \frac{1}{P} \sum_{p=1}^{p=P} N_{\text{OL},p}, \quad \bar{N}_{\text{Edge}} = \frac{1}{P} \sum_{p=1}^{p=P} N_p, \quad (10)$$

where  $N_p$  and  $N_{\text{OL},p}$  (subscript OL like overlapping) are the number of edges of the block and enlarged block  $p$ , respectively. In Eq. (9), the exponent 3 corresponds to the complexity of LU decompositions made on the blocks and the term  $\mathcal{O}(\bar{N}_{\text{Edge}} \bar{N}_{\text{Edge,OL}})$  is related to the calculation of the matrix-vector products. If the two matrices of the LU decomposition of the submatrix  $\bar{\mathbf{Z}}_{i',i'}$  can be stored, the complexity in Eq. (9) becomes

$$\begin{aligned} C_{\text{SDIM}} \approx & P \mathcal{O}(\bar{N}_{\text{Edge,OL}}^3) + \left[ (K_{\text{SDIM}} + 1) P \mathcal{O}(\bar{N}_{\text{Edge,OL}}^2) \right] \\ & + K_{\text{SDIM}} P(P-1) \mathcal{O}(\bar{N}_{\text{Edge}}^2), \end{aligned} \quad (11)$$

where  $\bar{N}_{\text{Edge}} \bar{N}_{\text{Edge,OL}} \approx \bar{N}_{\text{Edge}}^2$ . Compared to a LU direct inversion of the whole impedance matrix of complexity

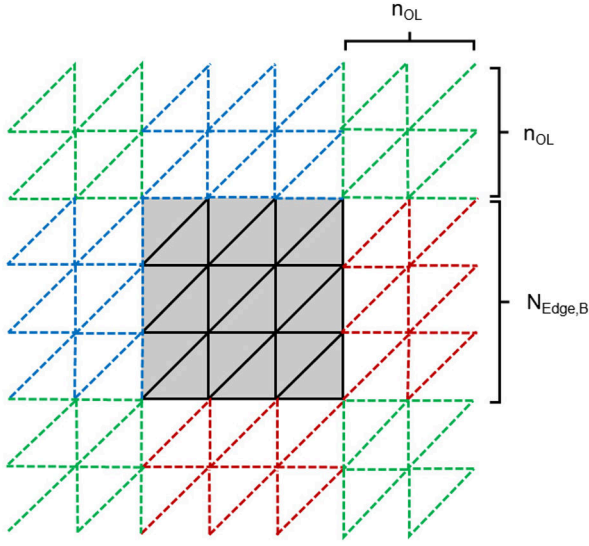


**Fig. 2.** For a given block, positions of the corner (green), top (blue), left (blue), bottom (red), and right (red) blocks of the overlapped blocks. Edges also are shown and overlapping is the same with respect to the  $x$  and  $y$  directions.

$\mathcal{O}((\sum_{i=1}^P N_i)^3)$ , the time savings is significant. The integer  $N_{OL,p}$  equals the number of edges of the original block  $p$ ,  $N_p$ , plus the overlapped edges  $n_{OL}$ . Without loss of generality, this number is assumed to be the same with respect to the directions  $x$  and  $y$  of the surface. The same assumption is done on the number of blocks  $N_{Block} = N_{Block,x} N_{Block,y} = P$ .

The exceed edges owing to overlapping is determined from Fig. 2. First, the number of blocks that interact with the adjacent blocks are counted according to their relative position. From Fig. 2, the total number of corner blocks is  $N_{Corner} = 4(N_{Block,x} - 1)(N_{Block,y} - 1)$ , the total number of top and bottom blocks is  $N_{T,B} = 2(N_{Block,y} - 1)N_{Block,x}$ , and the total number of left and right blocks is  $N_{L,R} = 2(N_{Block,x} - 1)N_{Block,y}$ . In addition, Fig. 2 shows that the number of edges associated to one corner is  $3n_{OL}^2$  (in green dashed line), the number of edges (in blue dashed line) associated either to the top or left position is  $3N_{Edge,B}n_{OL} - n_{OL}$ , and that (in red dashed line) associated to either the bottom or right position is  $3N_{Edge,B}n_{OL} - n_{OL} - N_{Edge,B}$ . For subsurfaces of the same area ( $N_{Block,x} = N_{Block,y} = \sqrt{P}$ ) and  $n_{OL} > 0$ , the excess of edges is then

$$N_{Edge,OL} - N_{Edge} = 12(\sqrt{P} - 1)^2 n_{OL}^2 + 2(\sqrt{P} - 1) \times \sqrt{P}(6N_{Edge,B}n_{OL} - 2n_{OL} - N_{Edge,B}). \quad (12)$$

In addition,  $N_{Edge,B} = (\sqrt{N_{Vertex}} - 1)/\sqrt{P} \approx \sqrt{N_{Edge}/3}/\sqrt{P}$  ( $N_{Edge} \approx 3N_{Vertex}$ ). In practice,  $n_{OL} \ll N_{Edge,B}$ , which implies that

$$N_{Edge,OL} - N_{Edge} \approx (\sqrt{P} - 1) \times \left[ 12(\sqrt{P} - 1)n_{OL}^2 + 2\sqrt{\frac{N_{Edge}}{3}}(6n_{OL} - 1) \right]. \quad (13)$$

This exceed is proportional to  $12Pn_{OL}^2$  and  $6.9\sqrt{P}N_{Edge}n_{OL}$ .

The SDIM storage complexity,  $M_{SDIM}$ , is similar to that of the brute force MoM and equals  $N_{Edge,OL}^2$ . It corresponds to the storage of the  $P$  submatrices  $\{\bar{\mathbf{Z}}_{i',i'}\}$  and  $P(P-1)$  submatrices  $\{\bar{\mathbf{Z}}_{i',i_2}\}$  (with  $i_1 \neq i_2$ ). We will show that ACA allows us to reduce this complexity, thanks to the compression of the  $P(P-1)$  coupling submatrices.

### C. CBFM

Like SDIM, the CBFM begins by dividing the geometry of the object to analyze into  $P$  blocks. Next, a PBF is computed for each block by solving the linear system,

$$\bar{\mathbf{Z}}_{i',i'} \mathbf{Y}_{i',k_{IPW}}^{(0)} = \mathbf{B}_{i',k_{IPW}}, \quad (14)$$

where the subscript prime indicates that the block  $i$  is enlarged and  $k_{IPW}$  stands for the  $k_{IPW}$ th plane wave (ranging from 1 to  $2N_{IPW,i}$ ). The original version of CBFM [18] used  $\mathbf{B}_{i',k_{IPW}} = \mathbf{b}_{i'}$  (single incident plane wave,  $k_{IPW} = 1$ ) and SBFs are calculated. In 2008 [31], another way is proposed to calculate the PBFs and the computation of SBFs is not required. In [30], for a 2D rough surface, it is shown that the original CBFM method lacks precision.

Lucente *et al.* [31] solved the linear system in Eq. (14) from a collection of  $2N_{IPW,i}$  bipolarized incident plane waves  $\{\mathbf{B}_{i',k_{IPW}}\}$ , and the resulting vectors  $\{\mathbf{Y}_{i',k_{IPW}}^{(0)}\}$  are stored in a matrix  $\bar{\mathbf{J}}_i$  of size  $N_{Edge,i} \times 2N_{IPW,i}$ , where  $N_{Edge,i}$  is the number of edges of the block  $i$  without overlapping. The results show that the overlapped edges of  $\mathbf{Y}_{i',k_{IPW}}^{(0)}$  are removed.

The choice of  $N_{IPW,i}$  must be relevant to avoid making the matrix too big. The redundant information due to the over-estimation of  $N_{IPW,i}$  is eliminated via the use of a truncated singular value decomposition (SVD). It means that from a given threshold  $\epsilon_{CBFM,SVD}$ , the values, for which the moduli of the normalized eigenvalues are smaller than  $\epsilon_{CBFM,SVD}$ , are removed. The size of  $\bar{\mathbf{J}}_i$  becomes  $N_{Edge,i} \times N_{IPW,SVD,i}$  with  $N_{IPW,SVD,i} < 2N_{IPW,i}$ .

The last stage of CBFM solves a reduced linear system  $\bar{\mathbf{Z}}^R \mathbf{a}^R = \mathbf{b}^R$  defined as

$$\begin{bmatrix} \bar{\mathbf{Z}}_{1,1}^R & \bar{\mathbf{Z}}_{1,2}^R & \cdots & \bar{\mathbf{Z}}_{1,P}^R \\ \bar{\mathbf{Z}}_{2,1}^R & \bar{\mathbf{Z}}_{2,2}^R & \cdots & \bar{\mathbf{Z}}_{2,P}^R \\ \vdots & \vdots & \ddots & \vdots \\ \bar{\mathbf{Z}}_{P,1}^R & \bar{\mathbf{Z}}_{P,2}^R & \cdots & \bar{\mathbf{Z}}_{P,P}^R \end{bmatrix} \begin{bmatrix} \mathbf{a}_1^R \\ \mathbf{a}_2^R \\ \vdots \\ \mathbf{a}_P^R \end{bmatrix} = \begin{bmatrix} \mathbf{b}_1^R \\ \mathbf{b}_2^R \\ \vdots \\ \mathbf{b}_P^R \end{bmatrix}, \quad (15)$$

where the submatrix  $\bar{\mathbf{Z}}_{i,j}^R$  and the subvector  $\mathbf{b}_i^R$  are defined as

$$\begin{cases} \bar{\mathbf{Z}}_{i,j}^R = \bar{\mathbf{J}}_i^H \bar{\mathbf{Z}}_{i,j} \bar{\mathbf{J}}_j [N_{IPW,SVD,i} \times N_{IPW,SVD,j}] \\ \mathbf{b}_j^R = \bar{\mathbf{J}}_j^H \mathbf{b}_j [N_{IPW,SVD,i} \times 1] \end{cases}. \quad (16)$$

Moreover, the symbol H stands for the conjugate transpose operator and the indexes  $i$  and  $j$  go from 1 to  $P$ . The vector  $\mathbf{a}_i$  of Eq. (5) is equal to  $\mathbf{a}_i = \bar{\mathbf{J}}_i \mathbf{a}_i^R$ .

The problem is then represented by the characteristic square matrix of size  $(P\bar{N}_{\text{IPW,SVD}})^2$  instead of a square matrix of size  $N_{\text{Edge}}^2 = (P\bar{N}_{\text{Edge}})^2$ , where  $\bar{N}_{\text{IPW,SVD}} = (1/P)\sum_{p=1}^P N_{\text{IPW,SVD},p}$ . If multiple excitations  $\{\mathbf{b}\}$  (for instance, a monostatic case) are calculated, then  $\bar{\mathbf{Z}}^{\text{R}}$  (or the two matrices of the LU decomposition) and  $\{\mathbf{J}_i\}$  (required to calculate  $\mathbf{b}_i$ ) must be stored, corresponding to store  $(P\bar{N}_{\text{IPW,SVD}})^2 + P\bar{N}_{\text{Edge}}\bar{N}_{\text{IPW,SVD}}$  complex numbers. The problem is then reduced by a factor  $\beta_1 > 1$  and equals

$$\frac{1}{\beta_1} = \frac{P^2\bar{N}_{\text{IPW,SVD}}^2 + P\bar{N}_{\text{Edge}}\bar{N}_{\text{IPW,SVD}}}{P^2\bar{N}_{\text{Edge}}^2} = \frac{1}{\beta_{\text{CBFM}}} \left( \frac{1}{\beta_{\text{CBFM}}} + \frac{1}{P} \right), \quad (17)$$

where  $\beta_{\text{CBFM}} = \bar{N}_{\text{Edge}}/\bar{N}_{\text{IPW,SVD}} > 1$ . If  $\beta_{\text{CBFM}} \gg 1$  and  $P \gg 1$ , the CBFM is very efficient for multiple excitations.

The complexity of the CBFM is expressed as

$$C_{\text{CBFM}} \approx P \left[ 2\mathcal{O}(\bar{N}_{\text{Edge,OL}}^3) + \bar{N}_{\text{IPW}}\mathcal{O}(\bar{N}_{\text{Edge,OL}}^2) \right] + 2P^2\bar{N}_{\text{IPW,SVD}}\mathcal{O}(\bar{N}_{\text{Edge}}^2) + \mathcal{O}(N_R^2) + \mathcal{O}(N_R^3), \quad (18)$$

where  $N_R = P\bar{N}_{\text{IPW,SVD}}$  and  $\bar{N}_{\text{IPW}} = (1/P)\sum_{p=1}^P N_{\text{IPW},p}$ . The first line corresponds to the calculation of the PBFs, in which the factor 2 comes from the LU decomposition and the truncated SVD.

## D. RACA

An ACA algorithm [23,24] is implemented to take advantage of the low-rank property of the off-diagonal submatrices  $\bar{\mathbf{Z}}_{i,j}$  ( $i \neq j$ ) representing two well-separated blocks. The ACA method approximates a dense matrix  $\bar{\mathbf{Z}}$  of size  $N \times M$  by a matrix–matrix product as

$$\bar{\mathbf{Z}} \approx \bar{\mathbf{U}}\bar{\mathbf{V}}, \quad (19)$$

where  $\bar{\mathbf{U}}$  is a matrix of size  $N \times r$  and  $\bar{\mathbf{V}}$  is a matrix of size  $r \times M$ , with  $r$  as the effective rank of  $\bar{\mathbf{Z}}$ . Clearly, the method requires the storage of only  $r \times (N + M)$  complex numbers and its computational complexity scales as  $\mathcal{O}(r^2(N + M))$ . The ACA compression is applied in Eq. (7) for the calculation of  $\mathbf{Y}_i^{(k)}$  ( $k > 0$ ), and in Eq. (16) for the computations of  $\{\bar{\mathbf{Z}}_{i,j}^{\text{R}}\}$ , in which the coupling matrices  $\{\bar{\mathbf{Z}}_{i,j}\}$  (with and without overlapping) are compressed.

To improve the compression [22,26,32], a QR decomposition is done both on matrices  $\bar{\mathbf{U}}$  and  $\bar{\mathbf{V}}$  and a truncated SVD is then applied by introducing a threshold  $\epsilon_{\text{ACA,SVD}}$ . Typically,  $\epsilon_{\text{ACA,SVD}} = 10\epsilon_{\text{ACA}}$ , where  $\epsilon_{\text{ACA}}$  is the ACA threshold ranging from  $10^{-5}$  to  $10^{-3}$ . In addition, the norm introduced to stop the ACA algorithm and modified in [26] is used. Chen *et al.* [22] proposed another method to calculate this norm by using both the QR decomposition of  $\bar{\mathbf{U}}$  and  $\bar{\mathbf{V}}$  in the loop over  $r$ . For our problem, numerical tests showed that this algorithm is less

efficient compared to what was used in [26]. Therefore, it is not applied in this paper.

As shown in Eq. (7) for the SDIM, the coupling matrices  $\{\bar{\mathbf{Z}}_{i',p}\}$  must be compressed. For a given coupling submatrix  $\bar{\mathbf{Z}}_{i',p}$ , the source and observation edges can be identical. Even if the size of the coupling submatrix is large, if some elements interact on the same edge (self-interaction), then the ACA compression is not efficient. It occurs for adjacent blocks. To solve this issue, these edges are removed, which has no impact on the SDIM precision.

To quantify the compression efficiency, the following SDIM mean compression rate is defined as

$$\bar{\tau}_{\text{SDIM}} = 1 - \left( \frac{\bar{N}_{\text{Edge,OL}}}{\bar{N}_{\text{Edge}}} \right)^2 \frac{1}{P(P-1)} \sum_{i=1}^{i=P} \sum_{j=1}^{j=P, j \neq i} \frac{r_{i,j}(n_i + m_j)}{m_i n_j}, \quad (20)$$

where the matrix  $\bar{\mathbf{Z}}_{i',j}$  has a size  $n_i \times m_j$  and a rank  $r_{i,j}$ . The factor  $(\bar{N}_{\text{Edge,OL}}/\bar{N}_{\text{Edge}})^2$  comes from the additional edges required due to overlapping. With the CBFM, the overlapping is not required for the coupling matrices, which implies that  $\bar{N}_{\text{Edge,OL}}/\bar{N}_{\text{Edge}} = 1$  and  $\bar{\tau}_{\text{SDIM}} < \bar{\tau}_{\text{CBFM}}$ .

IFRACA is applied, then the SDIM in Eq. (11) complexity is

$$C_{\text{SDIM}} \approx P\mathcal{O}(\bar{N}_{\text{Edge,OL}}^3) + \left[ (K_{\text{SDIM}} + 1)P\mathcal{O}(\bar{N}_{\text{Edge}}^2) + K_{\text{SDIM}}P(P-1)\mathcal{O}(\bar{N}_{\text{Edge}}^2)(1 - \bar{\tau}_{\text{SDIM,RACA}}) \right], \quad (21)$$

and that of CBFM remains nearly unchanged; that is,

$$C_{\text{CBFM,RACA}} \approx C_{\text{CBFM}} = \text{Equation (18)}. \quad (22)$$

## 3. NUMERICAL RESULTS

The SDIM convergence order  $K_{\text{SDIM}}$  is determined for a threshold  $\epsilon_{\text{SDIM}} = 10^{-2}$ . The surface has a Gaussian height distribution and its autocorrelation function is also Gaussian. The surface area is defined as  $A_0 = L_x \times L_y = L_x^2$  ( $L_y = L_x$ ),  $\sigma_z$  stands for the surface height standard deviation and  $\{L_{c,x}, L_{c,y} = L_{c,x}\}$  are the correlation lengths with respect to the  $x$  and  $y$  directions, respectively.

This section compares the NRCS computed from SDIM, CBFM, SDIM + RACA, and CBFM + RACA by considering a randomly rough surface. First, the surface area is  $(12\lambda_0)^2$  to compare with results obtained from a direct LU decomposition of the whole matrix (reference solution), where  $\lambda_0$  is the wavelength in free space. A parametric study is also addressed versus the incidence angle  $\theta_i$ , the ratios  $\sigma_z/\lambda_0$  and  $L_{c,x}/\lambda_0$  ( $L_{c,y} = L_{c,x}$ ), and the polarizations. Next, the surface area is  $(24\lambda_0)^2$  to compare the efficiency of the two methods. In addition, the last subsection addresses the complexity of the two methods. The extent of the Braunish *et al.* [34] tapered wave is  $g = L_x/4$  (surface of area  $L_x^2$ ).

### A. Surface Area of $(12\lambda_0)^2$ and without RACA

The incidence angles are  $\theta_{\text{inc}} = \pi/6$ ,  $\phi_{\text{inc}} = 0$ , the azimuthal scattering angle is  $\phi_{\text{sca}} = 0$ , and the polarizations are VV (same

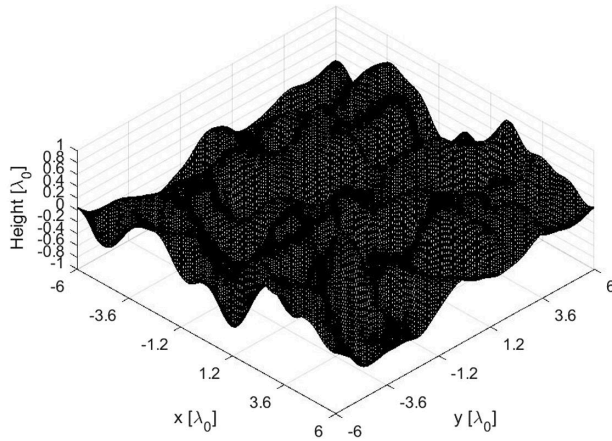


**Fig. 3.** Surface height versus the coordinates  $x$  and  $y$ . Surface area is  $L_x \times L_y = (12\lambda_0)^2$ ,  $\sigma_z = 0.3\lambda_0$ , and  $L_{c,x} = L_{c,y} = 1.5\lambda_0$ . The number of edges is  $N_{\text{Edge}} = 42,960$ , and the edge mean length is  $0.12\lambda_0$ .

as the reception and emission); in addition,  $\sigma_z/\lambda_0 = 0.3$  and  $L_{c,x}/\lambda_0 = L_{c,y}/\lambda_0 = 0.3$ . These parameters are chosen to have a moderate surface slope standard deviations with respect to the  $x$  and  $y$  directions slopes defined as  $\sigma_{s,x} = \sigma_{s,y} = \sqrt{2}\sigma_z/L_{c,x} = \sqrt{2}\sigma_z/L_{c,y} = 1/\sqrt{2} \approx 0.283$ . Figure 3 plots the corresponding surface height versus the coordinates  $x$  and  $y$ . The purpose is to produce reflections on the surface, which involves interactions between the blocks. The sampling with respect to the  $x$  and  $y$  directions are  $\Delta x = \Delta y = 0.1\lambda_0$ , which gives  $N_{\text{Edge}} = 42,960$  and the edge mean length is  $0.12\lambda_0$ .

Figure 4 plots the  $\text{NRCS}_{\text{SDIM}}$  in dB scale, computed from SDIM, versus the scattering angles and for different values of the number of blocks  $P$  with  $n_{\text{OL}} = 2$ . To highlight the difference, Fig. 5 plots the corresponding ratio  $\text{NRCS}_{\text{SDIM}}/\text{NRCS}_{\text{LU}}$  in dB scale versus the scattering angles, where  $\text{NRCS}_{\text{LU}}$  is the reference solution obtained from a direct LU decomposition of the whole matrix.

The legend indicates “SDIM ( $K_{\text{SDIM}}$ ),  $P$ ,  $t$ , RRE, DIF”, where  $K_{\text{SDIM}}$  is the convergence order,  $P$  the number of blocks,  $t$  the computing time (submatrices filling not included), and the relative residual error (RRE) defined as

$$\text{RRE} = \frac{\| \mathbf{E}_{\text{sca}}^{(K_{\text{SDIM}})} - \mathbf{E}_{\text{sca,LU}} \|_{\theta_{\text{sca}} \in [-\pi/2; \pi/2]}}{\| \mathbf{E}_{\text{sca,LU}} \|_{\theta_{\text{sca}} \in [-\pi/2; \pi/2]}} \quad (23)$$

where  $\mathbf{E}_{\text{sca}}$  is the scattered far field versus  $\theta_s$ . In addition, DIF stands for the mean absolute value of the ratio in dB scale defined as

$$\text{DIF} = \frac{1}{N_{\theta_{\text{sca}}}} \sum_{N_{\theta_{\text{sca}}}} 20 \left| \log_{10} \left| \frac{\mathbf{E}_{\text{sca}}^{(K_{\text{SDIM}})}}{\mathbf{E}_{\text{sca,LU}}} \right| \right| \quad (24)$$

where  $N_{\theta_{\text{sca}}}$  is the number of scattering angles.

As we can see, the results are in perfect agreement with those computed from LU, except for scattering angles  $\theta_{\text{sca}}$  near  $\pi/2$ , over which the NRCS strengths are very low. As  $P$  increases,  $K_{\text{SDIM}}$  increases because more iterations are required to account for all the interactions between the blocks and to vanish the fictitious currents produced by the block edges. In addition,

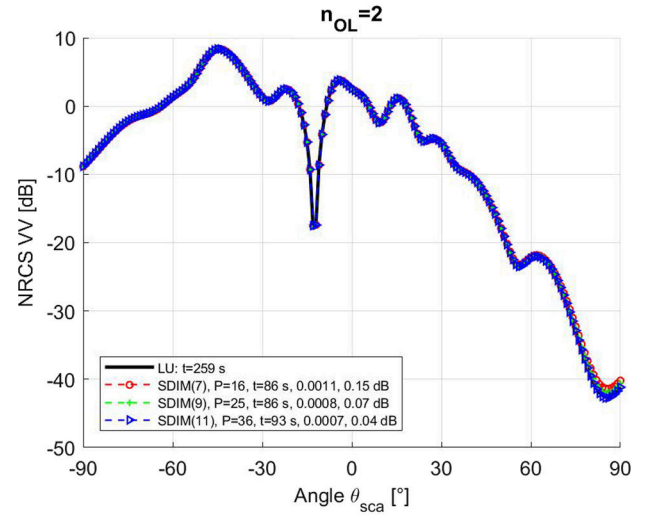


**Fig. 4.**  $\text{NRCS}_{\text{SDIM}}$  in dB scale computed from SDIM versus the scattering angles and for different values of the number of blocks  $P$  with  $n_{\text{OL}} = 2$ .

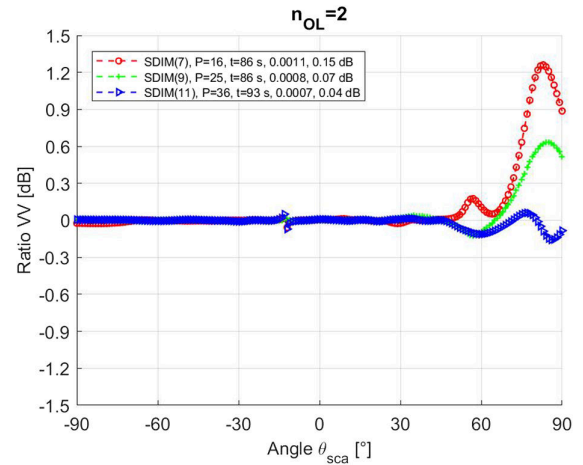


**Fig. 5.** Ratio  $\text{NRCS}_{\text{SDIM}}/\text{NRCS}_{\text{LU}}$  in dB scale computed from SDIM versus the scattering angles. Same parameters as in Fig. 4.

the time  $t$  increases and it is smaller than that obtained from LU. The difference is not significant because the size problem is rather small and, in MATLAB, the LU decomposition is parallelized.

Figure 6 plots the ratio  $\text{NRCS}_{\text{SDIM}}/\text{NRCS}_{\text{LU}}$  in dB scale versus the scattering angles and for different values of the overlapping  $n_{\text{OL}}$  with  $P = 25$ . As we can see, as  $n_{\text{OL}}$  increases, the SDIM convergence order decreases because less iterations are needed to vanish the fictitious currents produced by the block edges. The RRE value also decreases. Nevertheless, as shown by Eq. (13), a trade-off must be found between  $n_{\text{OL}}$  and  $K_{\text{SDIM}}$  because the number of total edges with overlapping increases with  $n_{\text{OL}}$ . For instance, for  $n_{\text{OL}} = \{0, 1, 2, 3\}$ ,  $N_{\text{Edge,OL}} = \{42,960; 47,872; 54,128; 60,768\}$ .

For CBFM, the number of plane waves  $N_{\text{PW}}$  is chosen as [35,36]

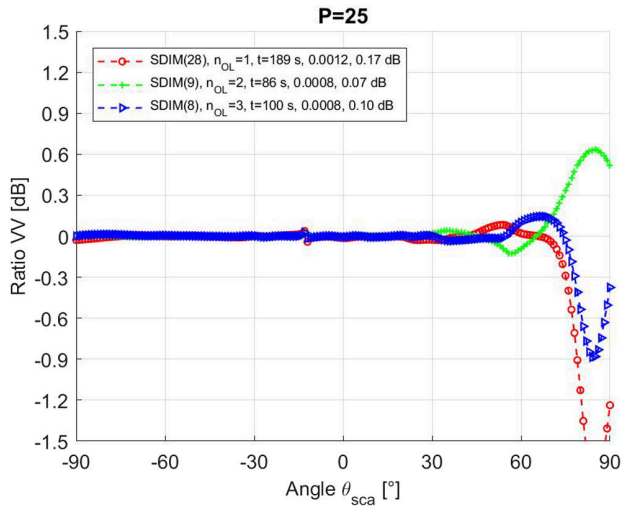
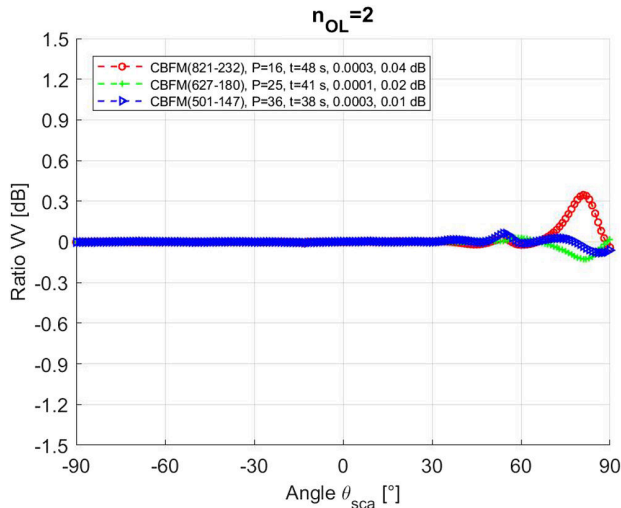


**Fig. 6.** Ratio  $\text{NRCS}_{\text{SDIM}}/\text{NRCS}_{\text{LU}}$  in dB scale computed from SDIM versus the scattering angles. Same parameters as in Fig. 4 but the integer  $n_{\text{OL}}$  changes and  $P = 25$ .

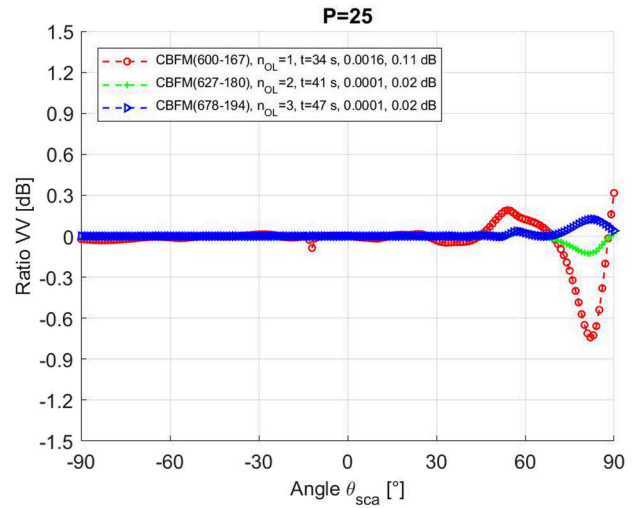
$$N_{\text{IPW}} = \left\lfloor \frac{2(kr_0 + 2\pi)^2}{n_{\text{IPW}}} \right\rfloor, \quad (25)$$

where the symbol  $\lfloor$  stands for the lower integer part and  $r_0$ , the sphere radius circumscribed to the block  $i$  of area  $L_{x,i}L_{y,i}$ , equals  $\sqrt{L_{x,i}^2 + L_{y,i}^2}/2$ . In addition, the integer  $n_{\text{IPW}} \geq 1$  is introduced because the simulations will show that  $N_{\text{IPW}}$  is overestimated. Equation (25) is related to the Nyquist sampling to ensure that there is no loss of information by decomposing any source into a sum of plane waves. The  $N_{\text{IPW}}$  plane waves are built from angles  $\theta \in [0; \pi/2]$  and  $\phi \in [0; 2\pi]$  with a constant sampling step  $\Delta\theta = \Delta\phi$ .

Figure 7 plots the ratio  $\text{NRCS}_{\text{CBFM}}/\text{NRCS}_{\text{LU}}$  in dB scale computed from CBFM versus the scattering angles and for different values of the number of blocks  $P$  with  $n_{\text{OL}} = 2$ ,  $\epsilon_{\text{CBFM,SVD}} = 10^{-3}$  and  $n_{\text{IPW}} = 2$  (a figure to compare with



**Fig. 7.** Ratio  $\text{NRCS}_{\text{CBFM}}/\text{NRCS}_{\text{LU}}$  in dB scale computed from CBFM versus the scattering angles and for different values of the number of blocks  $P$  with  $n_{\text{OL}} = 2$ ,  $\epsilon_{\text{CBFM,SVD}} = 10^{-3}$ , and  $n_{\text{IPW}} = 2$  (figure to compare with Fig. 5).



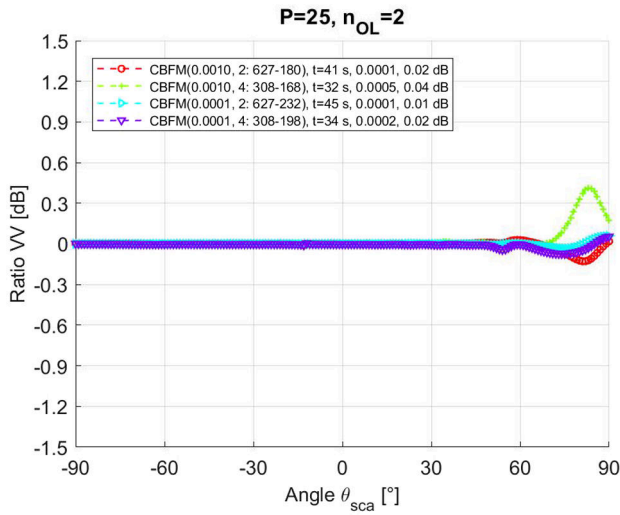
**Fig. 8.** Ratio  $\text{NRCS}_{\text{CBFM}}/\text{NRCS}_{\text{LU}}$  in dB scale computed from CBFM versus the scattering angles and for different values of the overlapping  $n_{\text{OL}}$ .  $P = 25$ ,  $\epsilon_{\text{CBFM,SVD}} = 10^{-3}$ , and  $n_{\text{IPW}} = 2$  (figure to compare with Fig. 6).

Fig. 5). The legend indicates “CBFM ( $2\bar{N}_{\text{IPW}} - \bar{N}_{\text{IPW,SVD}}$ ),  $P$ ,  $t$ , RRE, DIF”, where  $t$  is the computing time (submatrix filling not included),  $2\bar{N}_{\text{IPW}}$  is the mean value of the number of incidence bipolarized plane waves ( $N_{\text{IPW}}$  computed from Eq. (25) for a given block and multiplied by 2), and  $\bar{N}_{\text{IPW,SVD}}$  is that obtained after the truncated SVD. In addition, RRE and DIF are given by Eqs. (23) and (24), in which  $\mathbf{E}_{\text{sca}}^{(K_{\text{SDIM}})}$  is replaced by  $\mathbf{E}_{\text{sca,CBFM}}$ .

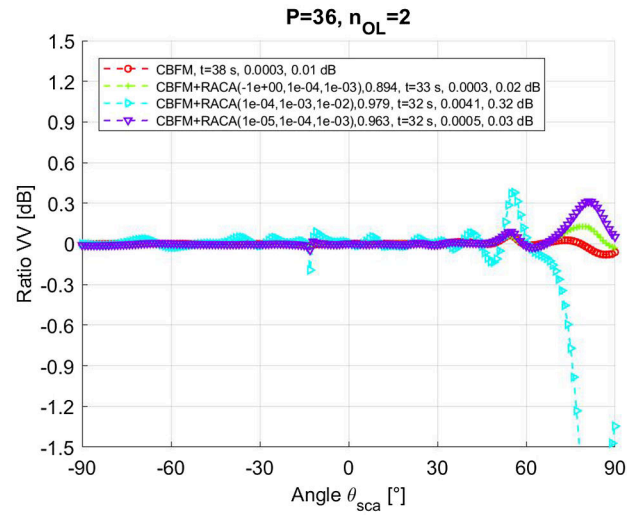
As we can see, as  $P$  increases, the RRE and DIF remain nearly constant. The square characteristic matrix  $\bar{\mathbf{Z}}^R$  has a size of  $P\bar{N}_{\text{IPW,SVD}} = \{3, 885; 4, 739; 5, 577\}$  for  $P = \{16, 25, 36\}$ . In Fig. 7, the time  $t$  should increase as  $P$  grows. In fact, the most expensive operation is the calculation of the PBFs; since  $P$  increases, the sizes of the submatrices decrease. It implies that the time spent to calculate their LU inversions decreases. For  $P = \{16, 25, 36\}$ , the reduction factor  $\beta_{\text{CBFM}} = \bar{N}_{\text{Edge}}/\bar{N}_{\text{IPW,SVD}} \approx \{11.6, 9.6, 8.1\}$ . For multiple excitations, it means that  $P$  should not be too large because the matrix  $\bar{\mathbf{Z}}^R$  must be stored.

Figure 8 plots the ratio  $\text{NRCS}_{\text{CBFM}}/\text{NRCS}_{\text{LU}}$  in dB scale computed from the CBFM versus the scattering angles and for different values of the overlapping  $n_{\text{OL}}$  ( $P = 25$ ,  $\epsilon_{\text{CBFM,SVD}} = 10^{-3}$ , and  $n_{\text{IPW}} = 2$ ) (a figure to compare with Fig. 6). As we can see, as  $n_{\text{OL}}$  increases, RRE and DIF decrease, but the number  $\bar{N}_{\text{IPW,SVD}}$  grows since the size of the overlapped blocks increases. It implies that the time  $t$  also increases.

Figure 9 plots the ratio  $\text{NRCS}_{\text{CBFM}}/\text{NRCS}_{\text{LU}}$  in dB scale computed from CBFM versus the scattering angles and for different values of  $\epsilon_{\text{CBFM,SVD}}$  and  $n_{\text{IPW}}$  ( $n_{\text{OL}} = 2$  and  $P = 36$ ). The legend indicates, “CBFM( $\epsilon_{\text{CBFM,SVD}}, n_{\text{IPW}}: 2\bar{N}_{\text{IPW}} - \bar{N}_{\text{IPW,SVD}}$ ),  $t$ , RRE, DIF”. As we can see, as  $n_{\text{IPW}}$  increases or/and  $\epsilon_{\text{CBFM,SVD}}$  decreases, the RRE does not change significantly. In addition, we can note that the truncated SVD allows a good value of  $\bar{N}_{\text{IPW,SVD}}$  to be obtained, even if the initial value of  $\bar{N}_{\text{IPW}}$  is chosen too large. The values  $\epsilon_{\text{CBFM,SVD}} = 10^{-3}$  and  $n_{\text{IPW}} = 2$  are a good choice and the use of the truncated



**Fig. 9.** Ratio  $\text{NRCS}_{\text{CBFM}}/\text{NRCS}_{\text{LU}}$  in dB scale computed from CBFM versus the scattering angles and for different values of  $\epsilon_{\text{CBFM,SVD}}$  and  $n_{\text{IPW}}$  ( $n_{\text{OL}} = 2$  and  $P = 36$ ).



**Fig. 11.** Ratio  $\text{NRCS}_{\text{CBFM}}/\text{NRCS}_{\text{LU}}$  in dB scale computed from CBFM + RACA versus the scattering angles and for different values of the RACA thresholds ( $n_{\text{OL}} = 2$ ,  $P = 36$ ,  $n_{\text{IPW}} = 2$ , and  $\epsilon_{\text{CBFM,SVD}} = 10^{-3}$ ).

SVD allows us to decrease the value of  $2\bar{N}_{\text{IPW}}$  to  $\bar{N}_{\text{IPW,SVD}}$  by a factor of the order of 3.3.

## B. Surface Area of $(12\lambda_0)^2$ with RACA

Figure 10 plots the ratio  $\text{NRCS}_{\text{SDIM}}/\text{NRCS}_{\text{LU}}$  in dB scale computed from SDIM + RACA versus the scattering angles and for different values of the RACA thresholds ( $n_{\text{OL}} = 2$  and  $P = 36$ ). For a given block, the adjacent blocks interact strongly, which means that the compression must be made with precision. Then, two RACA thresholds are defined: one for the near interactions (adjacent blocks),  $\epsilon_{\text{ACA},1}$ , and the second one, for the far interactions  $\epsilon_{\text{ACA},2}$ . In Fig. 10, the legend means, “SDIM( $K_{\text{SDIM}}$ )+RACA( $\epsilon_{\text{ACA},1}$ ,  $\epsilon_{\text{ACA},2}$ ,  $\epsilon_{\text{ACA,SVD}} = 10\epsilon_{\text{ACA},2}$ ),  $\bar{r}_{\text{SDIM}}$ ,  $t$ , RRE, DIF”, where  $\bar{r}_{\text{SDIM}}$  is the mean compression ratio (20),  $t$  is the computing time (filling matrices not

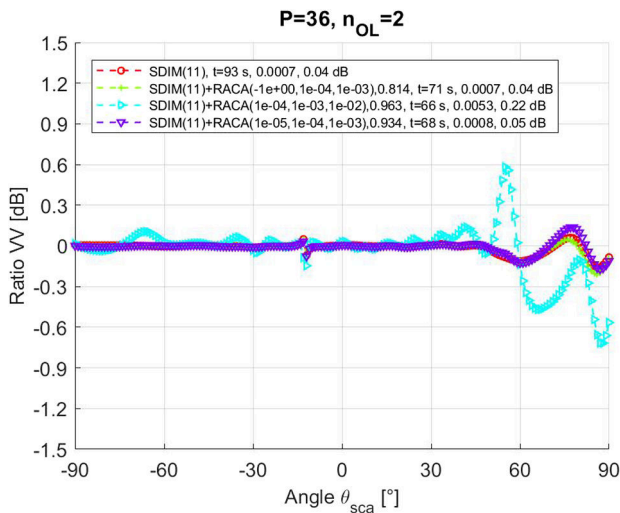


**Fig. 10.** Ratio  $\text{NRCS}_{\text{SDIM}}/\text{NRCS}_{\text{LU}}$  in dB scale computed from SDIM + RACA versus the scattering angles and for different values of the RACA thresholds ( $n_{\text{OL}} = 2$  and  $P = 36$ ).

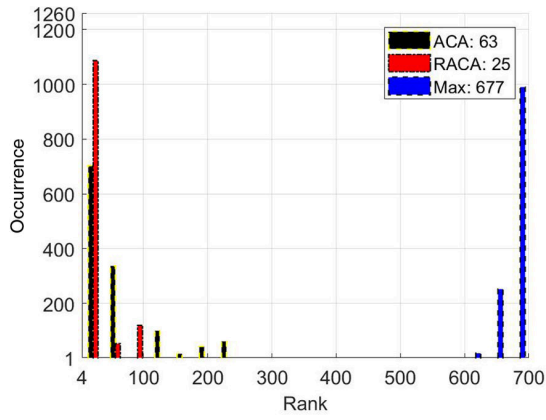
included), and RRE and DIF are defined by Eqs. (23) and (24). The value  $\epsilon_{\text{ACA},1} = -1$  means that ACA is not applied.

As we can see, the difference between SDIM + RACA and SDIM is small. As expected, if  $\epsilon_{\text{ACA},1}$  decreases, then the difference decreases and the computing time slightly grows, whereas the mean compression weakly decreases. Compared to SDIM, the time  $t$  decreases when RACA is applied, because the matrix-vector products are accelerated. For  $\epsilon_{\text{ACA},1} = -1$ , the results are nearly the same as those obtained for  $\epsilon_{\text{ACA},1} = 10^{-5}$ , which shows that it is relevant to apply RACA on the adjacent blocks since the mean compression is closer to 1.

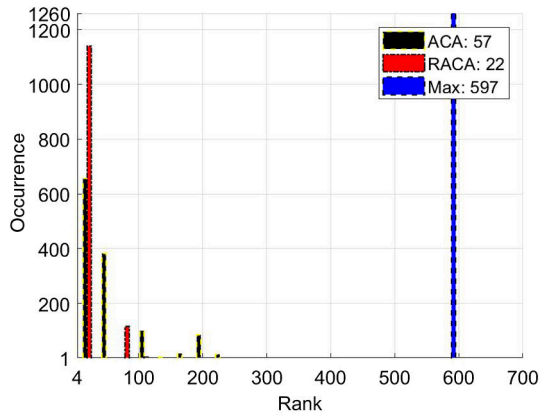
Figure 11 plots the ratio  $\text{NRCS}_{\text{CBFM}}/\text{NRCS}_{\text{LU}}$  in dB scale computed from CBFM + RACA versus the scattering angles and for different values of the RACA thresholds.  $n_{\text{OL}} = 2$ ,  $P = 36$ ,  $n_{\text{IPW}} = 2$  and  $\epsilon_{\text{CBFM,SVD}} = 10^{-3}$ . Compared to Fig. 10, the conclusions are the same on the RACA impact. Nevertheless, the mean compression is larger than that obtained with SDIM because there is no overlapping over the blocks. Then, ACA is more efficient. In addition, CBFM + RACA runs faster than SDIM + RACA like in Figs. 5–7 and Figs. 6–8.

Figure 12 plots the histogram of the SDIM coupling-submatrix ranks calculated from ACA and RACA, where  $\{\epsilon_{\text{ACA},1}, \epsilon_{\text{ACA},2}, \epsilon_{\text{ACA,SVD}}\} = \{10^{-5}, 10^{-4}, 10^{-3}\}$ . Figure 13 plots the same variations as in Fig. 12 but by considering the CBFM. In the legend, the label “Max” means that the rank equals  $r_{\text{max}} = n_i m_j / (n_i + m_j)$ , corresponding to the maximum value, for which ACA is not efficient for memory storage. The numbers  $(n_i, m_j)$  are the size of the submatrix to compress. In addition, in the legends of Figs. 12 and 13, the integer equals the mean value.

In Figs. 12 and 13, all the ranks are smaller than  $\{r_{\text{max}}\}$ , which means that all the submatrices are compressed. The ranks ranging from 100 to 200 corresponds to the submatrices adjacent to the current block. We can show that this number equals  $P_{\text{ACA,Near}} = 4 - 6(N_{x,\text{Block}} + N_{y,\text{Block}}) + 8N_{x,\text{Block}}N_{y,\text{Block}}$ . For  $N_{x,\text{Block}} = N_{y,\text{Block}} = \sqrt{P} = 6$ ,  $P_{\text{ACA,Near}} = 220$ . Although the



**Fig. 12.** Histogram of the SDIM coupling-submatrix ranks calculated from ACA and RACA, where  $\{\epsilon_{ACA,1}, \epsilon_{ACA,2}, \epsilon_{ACA,SVD}\} = \{10^{-5}, 10^{-4}, 10^{-3}\}$ .



**Fig. 13.** Histogram of the CBFM coupling-submatrix ranks calculated from ACA and RACA, where  $\{\epsilon_{ACA,1}, \epsilon_{ACA,2}, \epsilon_{ACA,SVD}\} = \{10^{-5}, 10^{-4}, 10^{-3}\}$ .

blocks are adjacent, the application of ACA is relevant. It is well known that ACA is efficient for far-field interactions, which explains why many ranks occur around the mean value, which is smaller than  $\bar{N}_{Edge} = 1193$  (mean value of edge numbers per block). The results also show that RACA is very efficient since the resulting rank is approximately divided by 3. The values are also more concentrated around the mean value. Note that  $\epsilon_{ACA,SVD} = 10\epsilon_{ACA,2}$  improves the compression without loss of precision.

The comparison of Fig. 12 to Fig. 13 also shows that ACA is more efficient for the CBFM, because there is no overlapping. Nevertheless, the final RCA mean rank is nearly the same between CBFM and SDIM.

Figures 14 and 15 plot the VH cross-polarized NRCSs in dB scale computed from SDIM + RACA and CBFM + RACA, respectively, versus the scattering angles and for different values of the RACA thresholds.  $n_{OL} = 2$  and  $P = 36$  (same simulation parameters as in Figs. 10 and 11). In addition, 20 dB is added to the NRCS to have comparable values to those of Fig. 4 (co-polarization VV). It explains why the cross polarization needs more precision than the VV ones. As we can see, the results

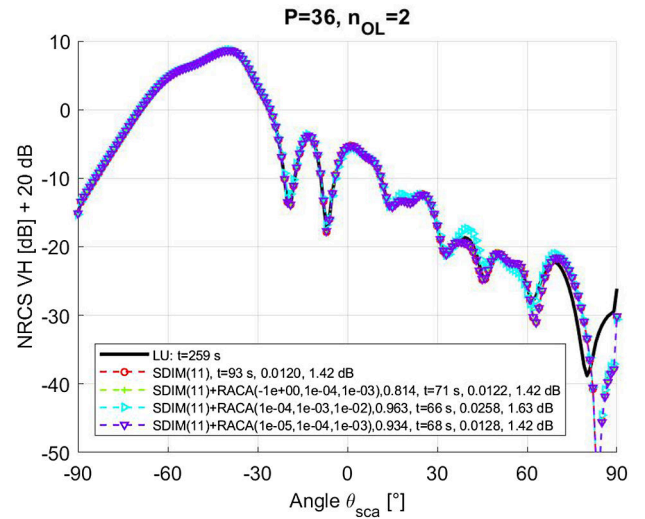


**Fig. 14.** NRCS<sub>SDIM</sub> in dB scale computed from SDIM + RACA versus the scattering angles and for different values of the RACA thresholds ( $n_{OL} = 2$  and  $P = 36$ ).

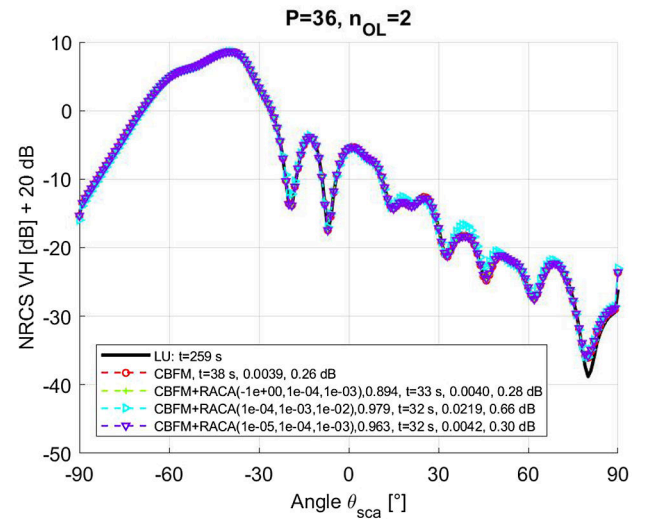


**Fig. 15.** NRCS<sub>CBFM</sub> in dB scale computed from CBFM + RACA versus the scattering angles and for different values of the RACA thresholds ( $n_{OL} = 2$ ,  $P = 36$ ,  $n_{IPW} = 2$ , and  $\epsilon_{CBFM,SVD} = 10^{-3}$ ).

match well with those obtained from LU except for low values of the NRCS, below  $40 + 20 = 60$  dB of the maximum of the VV NRCS.

### C. Surface Area of $(12\lambda_0)^2$ with RACA: Parametric Study

For SDIM + RACA and CBFM + RACA, Table 2 lists the values of DIF [dB] versus  $\theta_{inc}$  [°] and  $\sigma_z/\lambda_0$  for a given  $L_{c,x} = L_{c,y} = 1.5\lambda_0$ . The polarizations are VV. As we can see, the precision of the two methods has few sensitivities to  $\theta_{inc}$  and slightly increases as  $\sigma_z$  grows. In Table 2, the values 2.33 dB and 1.02 dB can appear large but, the plots (not depicted here) show that this corresponds to values 60 dB below the maximum.

**Table 2. DIF [dB] of SDIM + RACA-CBFM + RACA versus  $\theta_{\text{inc}}$  [°] and  $\sigma_z/\lambda_0$  (Polarizations Are VV)<sup>a</sup>**

	0	15	30	45
0.1	0.41–0.11	0.42–0.08	2.33–0.17	0.25–0.05
0.2	0.06–0.02	0.08–0.02	1.02–0.16	0.18–0.03
0.3	0.04–0.01	0.04–0.01	0.05–0.03	0.07–0.02

<sup>a</sup> $L_{c,x} = L_{c,y} = 1.5\lambda_0$ ;  $n_{\text{OL}} = 2$ ;  $P = 36$ ;  $\{\epsilon_{\text{ACA},1}, \epsilon_{\text{ACA},2}, \epsilon_{\text{ACA},\text{SVD}}\} = \{10^{-5}, 10^{-4}, 10^{-3}\}$ .

**Table 3. DIF [dB] of SDIM + RACA-CBFM + RACA versus  $\theta_{\text{inc}}$  [°] and  $\sigma_z/\lambda_0$  (Polarizations Are VH)<sup>a</sup>**

	0	15	30	45
0.1	3.98–2.42	3.72–1.23	2.70–0.97	1.63–1.11
0.2	1.22–0.51	3.33–0.41	1.39–0.26	1.61–0.39
0.3	0.52–0.18	1.14–0.16	1.42–0.30	0.98–0.24

<sup>a</sup> $L_{c,x} = L_{c,y} = 1.5\lambda_0$ ;  $n_{\text{OL}} = 2$ ;  $P = 36$ ;  $\{\epsilon_{\text{ACA},1}, \epsilon_{\text{ACA},2}, \epsilon_{\text{ACA},\text{SVD}}\} = \{10^{-5}, 10^{-4}, 10^{-3}\}$ .

The SDIM convergence order ranges from 8 to 11, has few sensitivities to  $\theta_i$ , and slightly increases as  $\sigma_z$  grows.

Table 3 lists the same values as in Table 2, but the polarizations are VH. Like the VV polarization, as  $\sigma_z$  grows, the methods are more accurate and CBFM gives better results.

Table 4 lists the same values as in Table 2 but the polarizations are HH. Compared to Table 2, the values are slightly larger for SDIM and the SDIM convergence order ranges from 8 to 13. It weakly increases with  $\theta_i$  and  $\sigma_z$ .

For SDIM + RACA and CBFM + RACA, Table 5 reports the same values as in Table 2, but  $\sigma_z = 0.3\lambda_0$  and  $L_{c,x}$  changes. As we can see, the two methods have few sensitivities to  $\theta_{\text{inc}}$  and  $L_{c,x}$ . In addition, the SDIM converges order ranges from 9 to 12 and decreases as  $L_{c,x}$  increases. For the VH polarizations (values not reported here), the value DIF increases as  $L_{c,x}$  increases and it has few sensitivities to  $\theta_i$ .

This section shows that CBFM is more accurate than SDIM, that the SDIM convergence order increases as  $L_{c,x}$  or  $\sigma_z$

**Table 4. DIF [dB] of SDIM + RACA-CBFM + RACA versus  $\theta_{\text{inc}}$  [°] and  $\sigma_z/\lambda_0$  (Polarizations Are HH)<sup>a</sup>**

	0	15	30	45
0.1	0.92–0.05	0.49–0.06	0.67–0.12	0.76–0.09
0.2	0.13–0.04	0.22–0.08	0.56–0.14	0.63–0.13
0.3	0.13–0.02	0.14–0.03	0.31–0.04	0.51–0.06

<sup>a</sup> $L_{c,x} = L_{c,y} = 1.5\lambda_0$ ;  $n_{\text{OL}} = 2$ ;  $P = 36$ ;  $\{\epsilon_{\text{ACA},1}, \epsilon_{\text{ACA},2}, \epsilon_{\text{ACA},\text{SVD}}\} = \{10^{-5}, 10^{-4}, 10^{-3}\}$ .

**Table 5. DIF [dB] of SDIM + RACA-CBFM + RACA versus  $\theta_{\text{inc}}$  [°] and  $\sigma_z/\lambda_0$  ( $\sigma_z = 0.3\lambda_0$  and  $L_{c,x}$  Changes)<sup>a</sup>**

	0	15	30	45
0.0	0.02–0.01	0.03–0.01	0.02–0.01	0.03–0.03
0.5	0.04–0.01	0.04–0.01	0.05–0.03	0.07–0.02
0.0	0.14–0.04	0.24–0.04	0.34–0.06	0.23–0.03

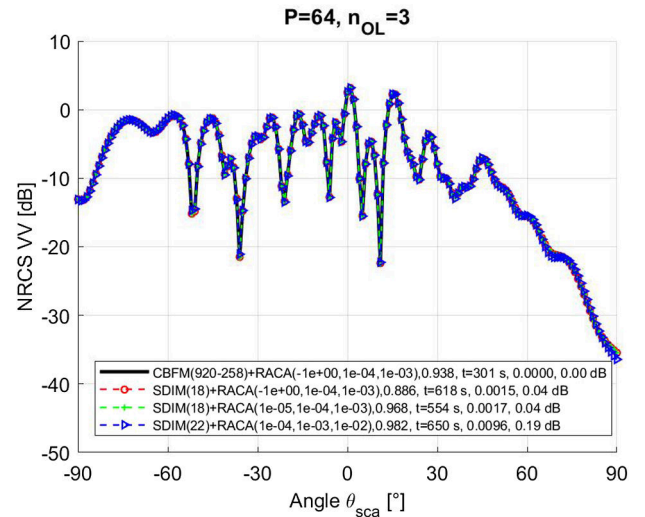
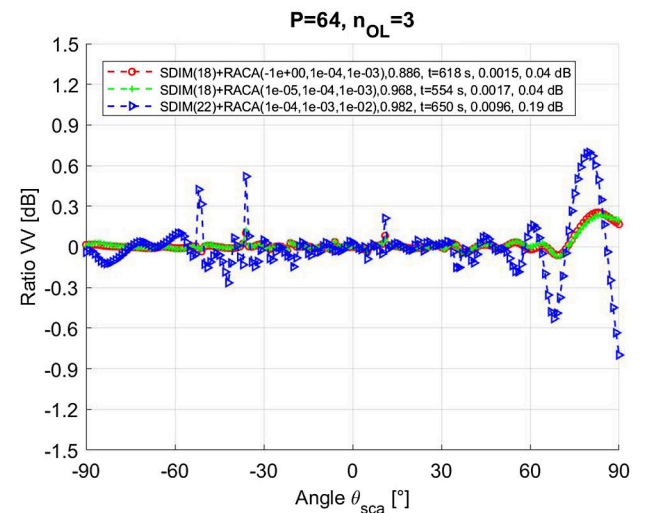
<sup>a</sup> $L_{c,x} = L_{c,y} = 1.5\lambda_0$ ;  $n_{\text{OL}} = 2$ ;  $P = 36$ ;  $\{\epsilon_{\text{ACA},1}, \epsilon_{\text{ACA},2}, \epsilon_{\text{ACA},\text{SVD}}\} = \{10^{-5}, 10^{-4}, 10^{-3}\}$ .

increases, and that it is larger for the HH polarization. In addition, the accuracy of SDIM increases as  $\sigma_z$  increases and  $L_{c,x}$  decreases. It is also important to underline that the stop criterion in Eq. (8) is defined over the surface currents and the precision of SDIM can be improved by decreasing the value of the threshold  $\epsilon_{\text{SDIM}}$ . The stop criterion could be defined over the scattered field, which would require radiation of the surface current at each order of SDIM.

#### D. Surface Area of $(24\lambda_0)^2$

In this subsection, the statistical parameters of the rough surface are  $L_{c,x} = L_{c,y} = 1.5\lambda_0$  and  $\sigma_z = 0.3\lambda_0$ , its area is  $(24\lambda_0)^2$ , the number of edges is 172,320 with an edge length mean value of  $0.118\lambda_0$ .

Figure 16 plots the NRCS in dB scale versus the scattering angles and for different values of  $\{\epsilon_{\text{ACA},1}, \epsilon_{\text{ACA},2}, \epsilon_{\text{ACA},\text{SVD}}\}$  ( $P = 64$  and  $n_{\text{OL}} = 3$ ). To highlight the difference, Fig. 17 plots

**Fig. 16.** NRCS in dB scale versus the scattering angles and for different values of  $\{\epsilon_{\text{ACA},1}, \epsilon_{\text{ACA},2}, \epsilon_{\text{ACA},\text{SVD}}\}$  ( $P = 64$  and  $n_{\text{OL}} = 3$ ).**Fig. 17.**  $\text{NRCS}_{\text{SDIM}}/\text{NRCS}_{\text{REF}}$  in dB scale versus the scattering angles with the same parameters as in Fig. 16.

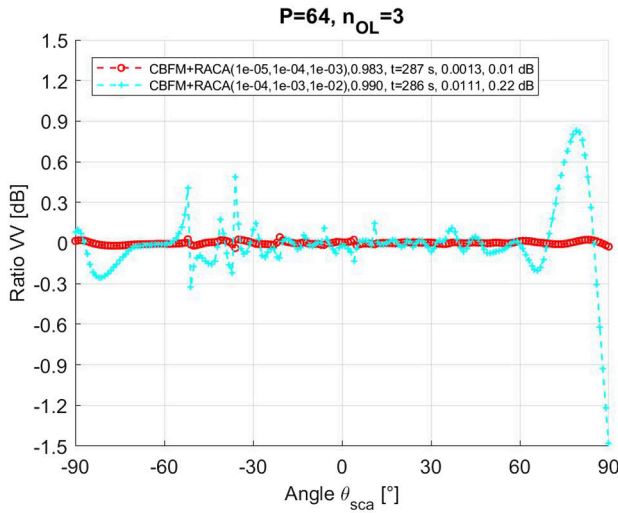


**Fig. 18.**  $\text{NRCS}_{\text{CBFM}}/\text{NRCS}_{\text{REF}}$  in dB scale versus the scattering angles and for different values of  $\{\epsilon_{\text{ACA},1}, \epsilon_{\text{ACA},2}, \epsilon_{\text{ACA},\text{SVD}}\}$  ( $P = 64$ ,  $n_{\text{OL}} = 3$ ,  $n_{\text{IPW}} = 2$ , and  $\epsilon_{\text{CBFM},\text{SVD}} = 10^{-3}$ ).

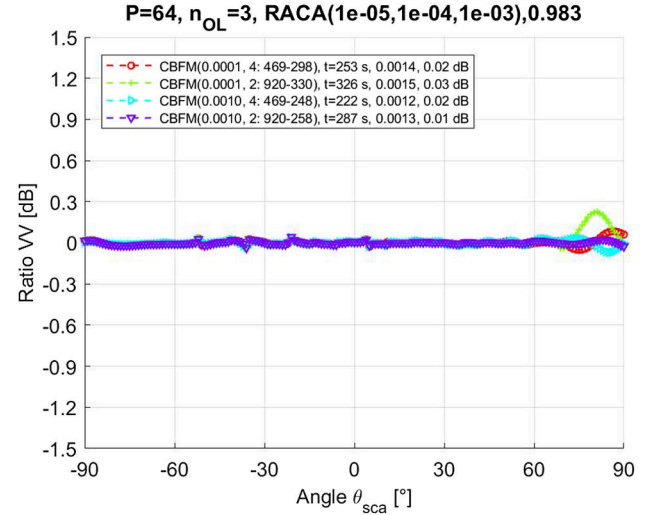
the corresponding NRCS ratio,  $\text{NRCS}_{\text{SDIM}}/\text{NRCS}_{\text{REF}}$ , in dB scale versus the scattering angles.  $\text{NRCS}_{\text{REF}}$  is obtained from CBFM with  $\{\epsilon_{\text{ACA},1}, \epsilon_{\text{ACA},2}, \epsilon_{\text{ACA},\text{SVD}}\} = \{-1, 10^{-4}, 10^{-3}\}$ ,  $n_{\text{IPW}} = 2$ , and  $\epsilon_{\text{CBFM},\text{SVD}} = 10^{-3}$ .

As we can see, the curves match well, which is in agreement with the results obtained for  $L_x = L_y = 12\lambda_0$ . When the RACA thresholds change, the computing time does not change significantly and the SDIM convergence order  $K_{\text{SDIM}}$  weakly increases. It means that the last orders of SDIM give a small contribution and are very sensitive to the precision of the coupling submatrices governed by the RACA thresholds. The SDIM threshold is  $10^{-2}$ . If this value increases, then the order  $K_{\text{SDIM}}$  decreases.

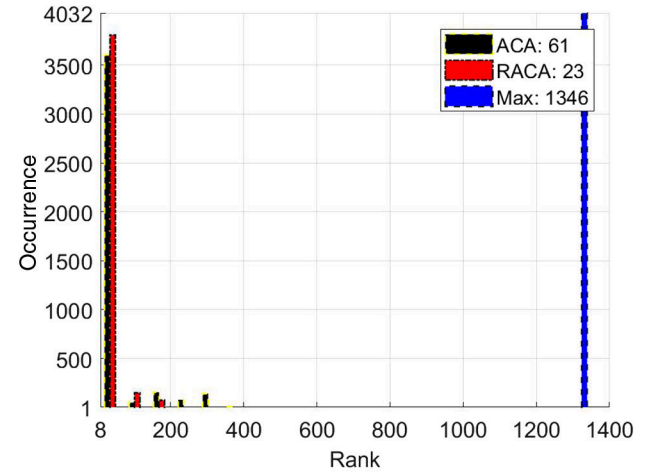
Figure 18 plots the ratio  $\text{NRCS}_{\text{CBFM}}/\text{NRCS}_{\text{REF}}$  in dB scale versus the scattering angles and for different values of  $\{\epsilon_{\text{ACA},1}, \epsilon_{\text{ACA},2}, \epsilon_{\text{ACA},\text{SVD}}\}$ . Like SDIM, the computing time has few sensitivities to the ACA thresholds and for  $\epsilon_{\text{ACA},1} = 10^{-4}$ , there are small differences that occur for scattering angles near  $\pi/2$ .

Figure 19 plots the ratio  $\text{NRCS}_{\text{CBFM}}/\text{NRCS}_{\text{REF}}$  in dB scale versus the scattering angles, and for different values of  $n_{\text{IPW}}$  and  $\epsilon_{\text{CBFM},\text{SVD}}$ . As we can see, the curves match well, except for low values of the NRCS. As the couple  $(2\bar{N}_{\text{IPW}}, \bar{N}_{\text{SVD},\text{IPW}})$  decreases ( $n_{\text{IPW}}$  grows or/and  $\epsilon_{\text{CBFM},\text{SVD}}$  increases), the computing time  $t$  (filling matrices not included) decreases. Like the case  $L_x = L_y = 12\lambda_0$ , the values  $n_{\text{IPW}} = 2$  and  $\epsilon_{\text{CBFM},\text{SVD}} = 10^{-3}$  are a good choice. It implies that the length of the reduced square matrix is  $\bar{N}_{\text{SVD},\text{IPW}} P = 16,512$ , giving a reduction factor  $\beta_{\text{CBFM}} = \bar{N}_{\text{Edge}}/\bar{N}_{\text{SVD},\text{IPW}} \approx 10.45$ .

Figure 20 plots the histogram of the CBFM coupling-submatrix ranks calculated from ACA and RACA.  $\{\epsilon_{\text{ACA},1}, \epsilon_{\text{ACA},2}, \epsilon_{\text{ACA},\text{SVD}}\} = \{10^{-5}, 10^{-4}, 10^{-3}\}$ . As we can see, the RACA improves the compression and the rank values are more concentrated around the mean value. Ranks ranging from 200 to 320 correspond to the adjacent blocks of number  $P_{\text{ACA},\text{Near}} = 420$ . In Fig. 13, the ratio  $\bar{r}_{\text{Max}}/\bar{r}_{\text{RACA}}$  (rank mean value given in the legend) is  $597/22 \approx 27.1$ ; whereas in



**Fig. 19.**  $\text{NRCS}_{\text{CBFM}}/\text{NRCS}_{\text{REF}}$  in dB scale versus the scattering angles and for different values of  $n_{\text{IPW}}$  and  $\epsilon_{\text{CBFM},\text{SVD}}$  ( $P = 64$ ,  $n_{\text{OL}} = 3$ , and  $\{\epsilon_{\text{ACA},1}, \epsilon_{\text{ACA},2}, \epsilon_{\text{ACA},\text{SVD}}\} = \{10^{-5}, 10^{-4}, 10^{-3}\}$ ).



**Fig. 20.** Histogram of the CBFM coupling-submatrix ranks calculated from ACA and RACA, where  $\{\epsilon_{\text{ACA},1}, \epsilon_{\text{ACA},2}, \epsilon_{\text{ACA},\text{SVD}}\} = \{10^{-5}, 10^{-4}, 10^{-3}\}$ .

Fig. 20, it is equal to  $1346/23 \approx 58.5$ , which shows that ACA is more efficient for a larger object. Indeed, the SDIM mean compression rate expressed by Eq. (20) can be approximated as

$$\bar{\tau}_{\text{SDIM}} \approx 1 - \left( \frac{\bar{N}_{\text{Edge,OL}}}{\bar{N}_{\text{Edge}}} \right)^2 \frac{\bar{r}_{\text{RACA}}}{\bar{r}_{\text{Max}}}, \quad (26)$$

in which  $\bar{N}_{\text{Edge,OL}}/\bar{N}_{\text{Edge}} = 1$  for the CBFM (no overlapping over the coupling submatrices).

## E. Complexity

Figure 21 plots the filling times of the submatrices in minutes. The surface length  $L_x = L_y$  ranges from  $12\lambda_0$  to  $27\lambda_0$  ( $\bar{N}_{\text{Edge}}$  ranges from 42,960 to 218,160). For LU, only the first three points are considered. The length of

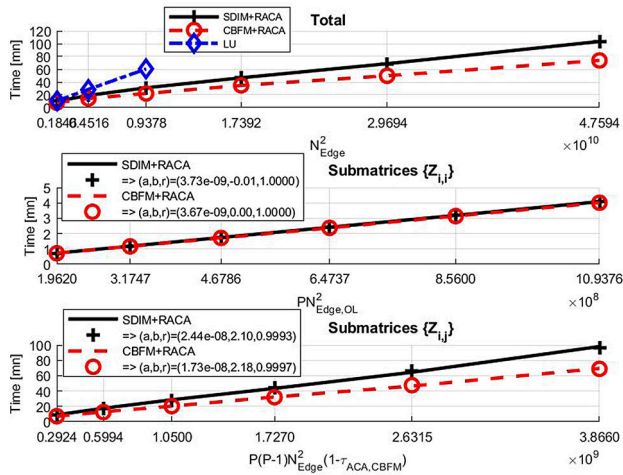


**Fig. 21.** Filling times of the submatrices in minutes. Top, total time versus  $N_{Edge}^2$ . Middle, time filling of the  $P$  impedance submatrices  $\{\bar{Z}_{i,i}\}$  versus  $P N_{Edge,OL}^2$ . Bottom, filling time of the  $P(P-1)$  coupling submatrices  $\{\bar{Z}_{i,j}\} (i \neq j)$  versus  $P(P-1) N_{Edge}^2 (1 - \bar{\tau}_{ACA,CBFM})$ . In addition, the last two subfigures plot the curves fitted by the equation  $y = ax + b$ , in which the values of  $a$ ,  $b$  and the correlation coefficient  $r$  are given in the legends.

the blocks is a constant that equals  $3\lambda_0$ , meaning that  $P$  ranges from  $4^2 = 16$  to  $9^2 = 81$ . For CBFM,  $n_{IPW} = 2$  and  $\epsilon_{CBFM,SVD} = 10^{-3}$ , and the RACA thresholds are  $\{\epsilon_{ACA,1}, \epsilon_{ACA,2}, \epsilon_{ACA,SVD}\} = \{10^{-5}, 10^{-4}, 10^{-3}\}$ .

The top of Fig. 21 plots the total time versus  $N_{Edge}^2$ . As we can see, the time of CBFM + RACA is approximately twice as small than that of SDIM + RACA because the mean compression rate is larger for CBFM + RACA. Compared to LU, the difference must be theoretically greater, but it depends on how the calling functions calculating the elements of submatrices are done. MATLAB software is used for the simulations, and the submatrices are computed in C language by using the mex library, which allows us to call the C function from MATLAB. When the impedance matrix of whole surface is calculated, the function is only called once; however, for the calculations of the submatrices, the same function is called  $P^2$  times. In addition, the RACA algorithm is written in MATLAB (call functions in C) and it can be significantly more time-consuming if the rank  $r$  is too large owing its complexity in  $\mathcal{O}(r^2(M+N))$ . The time needed can be significantly reduced if the submatrices are computed simultaneously by paralleling the code.

The middle of Fig. 21 plots the total time spent to calculate the  $P$  impedances submatrices  $\{\bar{Z}_{i,i}\}$  versus  $P N_{Edge,OL}^2$ . In addition, the curves are fitted by the equation  $y = ax + b$ , in which the values of  $a$ ,  $b$  and the correlation coefficient  $r$  are given in the legends. As we can see, the results perfectly match with its regression ( $r \approx 1$ ), meaning that the time is proportional to  $P N_{Edge,OL}^2$ .

The bottom of Fig. 21 plots the total time spent to calculate the  $P(P-1)$  coupling submatrices  $\{\bar{Z}_{i,j}\} (i \neq j)$  versus  $P(P-1) N_{Edge}^2 (1 - \bar{\tau}_{ACA,CBFM})$  and its linear regression. We assume that  $\bar{\tau}_{ACA,SDIM} \approx \bar{\tau}_{ACA,CBFM}$ . As we can see, the results match well with its regression ( $r \approx 0.999$ ), meaning that the

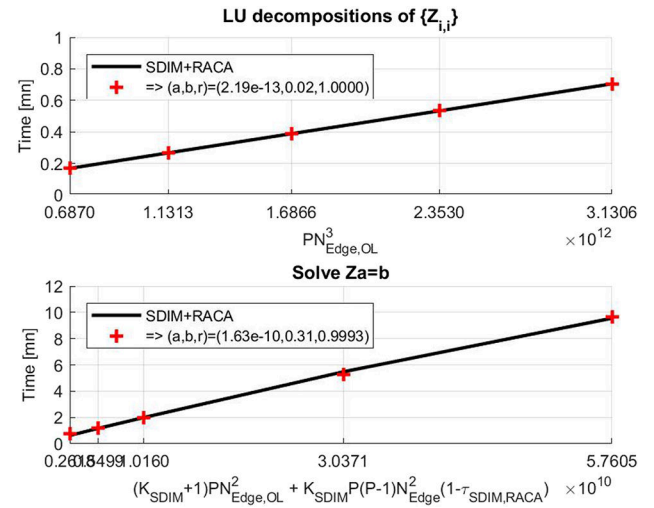


**Fig. 22.** Computing times in minute. Top, for the LU decompositions of  $\{\bar{Z}_{i,i}\}$  versus  $P N_{Edge,OL}^3$ . Bottom, to solve the linear system  $\bar{Z}\bar{a} = \bar{b}$  versus  $(K_{SDIM} + 1) P N_{Edge,OL}^2 + K_{SDIM} P(P-1) N_{Edge}^2 (1 - \bar{\tau}_{SDIM,RACA})$ . In addition, their regression is plotted.

time is proportional to  $P(P-1) N_{Edge}^2 (1 - \bar{\tau}_{ACA,CBFM})$ . In addition, the time is larger for the SDIM + RACA (its ACA mean compression rate is smaller than that of CBFM).

Figure 22 plots the computing time in minutes. At the top, there is the time for the LU decompositions of  $\{\bar{Z}_{i,i}\}$  versus  $P N_{Edge,OL}^3$ . At the bottom, you can see the time to solve the linear system  $\bar{Z}\bar{a} = \bar{b}$  versus  $(K_{SDIM} + 1) P N_{Edge,OL}^2 + K_{SDIM} P(P-1) N_{Edge}^2 (1 - \bar{\tau}_{SDIM,RACA})$ . In addition, their regression is plotted. As we can see, the results match well with their regression, which is in agreement with the complexity predicted by Eq. (11), in which the term  $P\mathcal{O}(N_{Edge,OL}^3)$  corresponds to the complexity of the LU decompositions of the  $P$  self-impedance submatrices.

Figure 23 plots the computing time in minutes related to the three stages of the CBFM algorithm. In addition, their regression is plotted. At the top, the time corresponds to the time spent to calculate the PBFs and it is plotted versus  $2P N_{Edge,OL}^3$ . In the

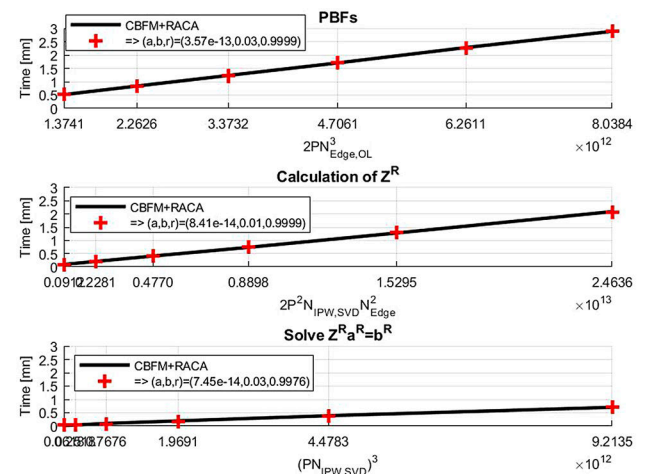


**Fig. 23.** Computing times in minutes related to three stages of the CBFM algorithm. In addition, their regression is plotted.

middle, the time corresponds to the time spent to calculate the reduced matrix  $\bar{\mathbf{Z}}^R$  and it is plotted versus  $2P^2\bar{N}_{\text{IPW,SVD}}\bar{N}_{\text{Edge}}^2$ . At the bottom, the time corresponds to the time spent to solve the linear system  $\bar{\mathbf{Z}}^R \mathbf{a}^R = \mathbf{b}^R$  and it is plotted versus  $N_R^3$ , where  $N_R = P\bar{N}_{\text{IPW,SVD}}$ . As we can see, the results match well with their regression, which is consistent with the theoretical complexity expressed by Eq. (18), in which only the higher-order terms are kept on for each step. In addition, as  $N_{\text{Edge}}$  increases, the most expensive operations are the calculations of the PBFs, next the reduced matrix  $\bar{\mathbf{Z}}^R$ .

#### 4. CONCLUSION

Two domain decomposition methods, SDIM and CBFM, have been investigated to calculate the scattered field from a 2D randomly rough surface.

For CBFM, numerical tests showed that in Eq. (25), the number of bipolarized plane waves  $2N_{\text{IPW}}$ , can be chosen with  $n_{\text{IPW}} = 2$  and the truncated SVD can be applied with a threshold of  $\epsilon_{\text{CBFM,SVD}} = 10^{-3}$ . The resulting reduction factor,  $\beta_{\text{CBFM}} = \bar{N}_{\text{Edge}}/\bar{N}_{\text{IPW,SVD}} \approx 10$ , where  $\bar{N}_{\text{IPW,SVD}}$  is approximately 3.5 times smaller than  $2N_{\text{IPW}}$ , which shows it is relevant to apply a truncated SVD. The number of overlapped edges by block,  $n_{\text{OL}}$ , must be two or three.

Numerical tests showed that SDIM is twice as slow as CBFM and is not able to efficiently treat several excitations, unlike CBFM. In addition, as the number of blocks increases, the SDIM convergence order  $K_{\text{SDIM}}$  increases. To remedy this issue,  $n_{\text{OL}}$  must increase, which grows the total number of edges. Typically,  $n_{\text{OL}}$  can be set as 10% of the size of the block.

The use of RACA makes the two methods more efficient in terms of complexity and memory storage, since the coupling-submatrices are compressed. Compared to a conventional ACA, the RACA allows the reduction of the mean rank by a factor 3, leading to a mean compression rate near 0.96–0.98 that increases as the problem size grows. Typically, the values of RACA thresholds can be chosen as  $\{\epsilon_{\text{ACA},1}, \epsilon_{\text{ACA},2}, \epsilon_{\text{ACA,SVD}}\} = \{10^{-5}, 10^{-4}, 10\epsilon_{\text{ACA},2}\}$ , where  $\epsilon_{\text{ACA},1}$  is the threshold for the compression of the adjacent blocks. For a precision of  $\pm 1$  dB, these values can be multiplied by 10.

It is also shown that the theoretical complexities of the two methods in Eqs. (11) and (18), are in very good agreement with those obtained numerically. It is important to underline that the time spent to calculate the  $P^2$  submatrices is approximately 90% of the total time, in which 80% is allocated for the computation of the  $P(P-1)$  coupling submatrices. A way to overcome this drawback would be to parallelize the code, which also would allow the acceleration of the calculations of  $\bar{\mathbf{Z}}^R$  (CBFM) and  $\bar{\mathbf{Y}}^{(k)}$  (SDIM).

**Disclosures.** The authors declare no conflicts of interest.

#### REFERENCES

1. L. Tsang, J. A. Kong, and K.-H. Ding, *Scattering of Electromagnetic Waves, Theories and Applications* (Wiley, 2000).

2. T. Elfouhaily and C.-A. Guérin, "Critical survey of approximate scattering wave theories from random rough surfaces (topical review)," *Waves Random Complex Media* **14**, R1–R40 (2004).
3. N. Pinel and C. Bourlier, *Electromagnetic Wave Scattering from Random Rough Surfaces—Asymptotic Models, Focus Series* (ISTE/Wiley, 2013).
4. C. Bourlier, *Radar Propagation and Scattering in a Complex Maritime Environment* (ISTE/Elsevier, 2018).
5. R. F. Harrington, *Field Computation by Moment Method* (Macmillan, 1968).
6. K. F. Warnick and W. C. Chew, "Numerical simulation methods for rough surface (topical review)," *Waves Random Complex Media* **11**, R1–R30 (2001).
7. M. Saillard and A. Sentenac, "Rigorous solutions for electromagnetic scattering from rough surfaces (topical review)," *Waves Random Complex Media* **11**, R103–R137 (2001).
8. W. C. Gibson, *The Method of Moments in Electromagnetics*, 2nd ed. (Chapman and Hall/CRC, 2008).
9. A. Quarteroni, R. Sacco, and F. Saverio, *Méthodes Numériques: Algorithmes, Analyse et Applications* (Springer-Verlag, 2007).
10. R. Coifman, V. Rokhlin, and S. Wandzura, "The fast multipole method for the wave equation: a pedestrian prescription," *IEEE Antennas Propag. Mag.* **35**(3), 7–12 (1993).
11. C.-C. Lu and W. C. Chew, "Fast far field approximation for calculating the RCS of large objects," *Microw. Opt. Technol. Lett.* **8**, 238–241 (1995).
12. S. W. Huang, G. H. Zhang, M. Y. Xia, and C. H. Chan, "Numerical analysis of scattering by dielectric random rough surfaces using modified SMCG scheme and curvilinear RWG basis functions," *IEEE Trans. Antennas Propag.* **57**, 3392–3397 (2009).
13. K. Pak, L. Tsang, and J. Johnson, "Numerical simulations and backscattering enhancement of electromagnetic waves from two-dimensional dielectric random rough surfaces with the sparse-matrix canonical grid method," *J. Opt. Soc. Am. A* **14**, 1515–1529 (1997).
14. L. Tsang, J. A. Kong, K.-H. Ding, and C. O. Ao, *Scattering of Electromagnetic Waves, Numerical Simulations* (Wiley, 2000).
15. L. Zhou, L. Tsang, V. Jandhyala, Q. Li, and C. H. Chan, "Emissivity simulations in passive microwave remote sensing with 3-D numerical solutions of Maxwell equations," *IEEE Trans. Geosci. Remote Sens.* **42**, 1739–1748 (2004).
16. T.-H. Liao, L. Tsang, S. Huang, N. Niamsuwan, S. Jaruwatanadilok, S.-B. Kim, H. Ren, and K.-L. Chen, "Copolarized and cross-polarized backscattering from random rough soil surfaces from L-band to Ku-band using numerical solutions of Maxwell's equations with near-field precondition," *IEEE Trans. Geosci. Remote Sens.* **54**, 651–662 (2016).
17. T. Qiao, L. Tsang, D. Vandemark, S. H. Yueh, T.-H. Liao, F. Nouguier, and B. Chapron, "Sea surface radar scattering at L-band based on numerical solution of Maxwell's equations in 3-D (NMM3D)," *IEEE Trans. Geosci. Remote Sens.* **56**, 3137–3147 (2018).
18. V. S. Prakash and R. Mitra, "Characteristic basis function method: a new technique for efficient solution of method of moments matrix equations," *Microw. Opt. Technol. Lett.* **36**, 95–100 (2003).
19. C. Bourlier, N. Pinel, and G. Kubické, "Propagation-inside-layer-expansion method combined with physical optics for scattering by coated cylinders, a rough layer, and an object below a rough surface," *J. Opt. Soc. Am. A* **30**, 1727–1737 (2013).
20. C. Bourlier, S. Bellez, and G. Kubické, "Sub-domain decomposition iterative method combined with ACA: an efficient technique for the scattering from a large highly conducting rough sea surface," *IEEE Trans. Antennas Propag.* **63**, 659–666 (2015).
21. S. Bellez, C. Bourlier, and G. Kubické, "An efficient PILE algorithm for solving the scattering from three-dimensional (3-D) nested homogeneous dielectric bodies," *J. Opt. Soc. Am. A* **32**, 392–401 (2015).
22. X. Chen, C. Gu, J. Ding, Z. Li, and Z. Niu, "Multilevel fast adaptive cross-approximation algorithm with characteristic basis functions," *IEEE Trans. Antennas Propag.* **63**, 3994–4002 (2015).
23. M. Bebendorf, "Approximation of boundary element matrices," *Numer. Math.* **86**, 565–589 (2000).
24. K. Zhao, M. N. Vouvakis, and J.-F. Lee, "The adaptive cross approximation algorithm for accelerated method of moments computations

- of EMC problems,” *IEEE Trans. Electromagn. Compat.* **47**, 763–773 (2005).
25. J. M. Tamayo, A. Heldring, and J.-M. Rius, “Multilevel adaptive cross approximation (MLACA),” *IEEE Trans. Antennas Propag.* **59**, 4600–4608 (2011).
26. A. Heldring, E. Ubeda, and J.-M. Rius, “On the convergence of the ACA algorithm for radiation and scattering problems,” *IEEE Trans. Antennas Propag.* **62**, 3806–3809 (2014).
27. C. Bourlier, “Low-grazing angle propagation and scattering by an object above a highly-conducting rough sea surface in a ducting environment from an accelerated MoM,” *Waves Random Complex Media* **28**, 724–742 (2018).
28. C. Li and R. Mittra, “Characteristic basis function method for fast analysis of 3-D scattering from objects buried under rough surfaces,” *IEEE Trans. Geosci. Remote Sens.* **57**, 5252–5265 (2019).
29. A. Yagbasan, C. A. Tunc, V. B. Erturk, A. Altintas, and R. Mittra, “Characteristic basis function method for solving electromagnetic scattering problems over rough terrain profiles,” *IEEE Trans. Antennas Propag.* **58**, 1579–1589 (2010).
30. Y. Arencibia Noa, C. Bourlier, G. Kubické, and S. Bellez, “Extended-SDIM: an efficient technique for rigorous evaluation of electromagnetic scattering by a 2D rough surface,” in *International Conference on Electromagnetics in Advanced Applications (ICEAA)*, Granada, Spain (IEEE, 2019).
31. E. Lucente, A. Monorchio, and R. Mittra, “An iteration-free MoM approach based on excitation independent characteristic basis functions for solving large multiscale electromagnetic scattering problems,” *IEEE Trans. Antennas Propag.* **56**, 999–1007 (2008).
32. A. Heldring, J. M. Rius, J. M. Tamayo, J. Parrón, and E. Ubeda, “Multiscale compressed block decomposition for fast direct solution of method of moments linear system,” *IEEE Trans. Antennas Propag.* **59**, 526–536 (2011).
33. W. T. Sheng, Z. Y. Shu, K. Yang, and M. S. Tong, “Efficient evaluation of weakly singular integrals arising from electromagnetic surface integral equations,” *IEEE Trans. Antennas Propag.* **61**, 3377–3381 (2013).
34. H. Braunisch, Y. Zhang, C. O. Ao, S.-E. Shih, Y. Eric Yang, K.-H. Ding, J. A. Kong, and L. Tsang, “Tapered wave with dominant polarization state for all angles of incidence,” *IEEE Trans. Antennas Propag.* **48**, 1086–1096 (2000).
35. I. Fenni, H. Roussel, M. Darces, and R. Mittra, “Fast analysis of large 3-D dielectric scattering problems arising in remote sensing of forest areas using the CBFM,” *IEEE Trans. Antennas Propag.* **62**, 4282–4291 (2014).
36. A. D. Yaghjian, “Sampling criteria for resonant antennas and scatterers,” *J. Appl. Phys.* **79**, 7472–7474 (1996).